PHYSICAL REVIEW B **109**, 235404 (2024)

Energy states of Rydberg excitons in finite crystals: From weak to strong confinement

Pavel A. Belov,[1] Florian Morawetz,[1] Sjard Ole Krüger,[1] Niklas Scheuler,[2] Patric Rommel,[2] Jörg Main,[2]
Harald Giessen,[3] and Stefan Scheel[1]
[1]*Institut für Physik, Universität Rostock, Albert-Einstein-Straße 23-24, 18059 Rostock, Germany*
[2]*Institut für Theoretische Physik I, Universität Stuttgart, Pfaffenwaldring 57, 70569 Stuttgart, Germany*
[3]*4th Physics Institute and Research Center SCoPE, Universität Stuttgart, Pfaffenwaldring 57, 70569 Stuttgart, Germany*

(Received 12 January 2024; revised 8 May 2024; accepted 22 May 2024; published 6 June 2024)

Due to quantum confinement, excitons in finite-sized crystals behave rather differently than in bulk materials. We investigate the dependence of energies of Rydberg excitons on the strengths of parabolic as well as rectangular confinement potentials in finite-sized crystals. The evolution of the energy levels of hydrogenlike excitons in the crossover region from weak to strong parabolic confinement is analyzed for different quantum numbers by numerical solution of the two-dimensional Schrödinger equation. The energy spectrum of hydrogenlike excitons in Cu_2O-based rectangular quantum wells is, in turn, obtained numerically from the solution of the three-dimensional Schrödinger equation as a function of the quantum well width. Various crossings and avoided crossings of Rydberg energy levels are observed and categorized based on the symmetry properties of the exciton wave function. Particular attention is paid to the two limiting cases of narrow and wide quantum wells attributed to strong and weak confinement, respectively. The energies obtained with the pure Coulomb interaction are compared with the results originating from the Rytova-Keldysh potential, i.e., by taking into account the dielectric contrast in the quantum well and in the barrier.

DOI: 10.1103/PhysRevB.109.235404

I. INTRODUCTION

Hydrogenlike systems are the bedrock of quantum theory, atomic physics as well as solid state physics. Rotational SO(3) symmetry as well as the hidden SO(4) symmetry properties of the hydrogen atom [1] imply high degeneracy of its energy levels. An external perturbation breaks the symmetry and lifts the degeneracy [2]. The nature of the perturbation can widely differ and can include, for example, external magnetic or electric fields [3–7], the influence of a third particle [8–10], or an artificial confining potential [11–13]. The latter is especially important for quantum optics, where confinement allows one to trap two-level and many-level systems into spatial lattices [14,15]. Thus quantum confinement is an essential tool which, on the one hand, makes it possible to localize quantum systems and, on the other hand, allows for the interaction of the localized objects [16].

In semiconductor physics, quantum confinement is a basic way to specify the properties of radiative quantum systems [11,17–20]. The strength of the confinement defines the distribution of energy levels and, thus, frequencies of the emitted light. Artificially grown heterostructures of GaAs, GaN, CdTe, and other materials provide a convenient framework for an experimental study of the influence of quantum confinement, namely the restriction of motion along one spatial dimension [13,21,22]. The potential profiles of the grown structures are usually modeled by simple quantum well (QW) potentials of rectangular [12], triangular [23,24], parabolic [25,26] or Pösch-Teller-like shapes [2]. Although the effect of such confinement on single-particle states is well-understood [27], the effect of confinement on few-body systems is more complicated [28]. The main point is that confinement of a two-body system requires solving a three-body Schrödinger equation [9,29–31], in which the confining potential plays the role of the third particle [32].

The confinement regime depends on the interplay between the size of the Rydberg state and the size of the QW. This means that, although for a given QW width the ground state of the size of the Bohr radius can be in a weak confinement regime (model of wide QW approaching the bulk crystal), a highly excited Rydberg exciton with a large principal quantum number can be strongly confined (model of narrow QW). The point is that if the mean size of the highly excited state is large enough, the state becomes squeezed in the QW. Even for the simplest model potentials, the crossover from weak to strong quantum confinement cannot be treated analytically. However, there are limiting, exactly solvable cases in the vicinity of which the perturbative treatment is accurate. For example, in the case of weak confinement, the Coulomb attraction dominates: the energy difference between quantum-confined energy levels is smaller than that between Coulomb bound states. Here, the quantum confinement can be treated as a small perturbation. The other limiting case is the strong confinement when, in turn, the Coulomb potential is treated as a small perturbation. In this case, the gaps between quantum-confined energies are much larger than the Rydberg energy of the Coulomb interaction. A crossover from strong to weak confinement and further to the bulk crystal allows one to follow the evolution of the energy levels, which provides an important insight for experimentalists to predict the energetic properties of their grown structures.

Practical examples of the effect of quantum confinement are cascade lasers. They include the well-known quantum cascade lasers [17] as well as recently realized bosonic cascade lasers [26]. GaAs-based heterostructures with a parabolic-like potential profile can be grown by a gradual change of the alloy concentration [33,34]. As a result, a series of equidistant quantum-confinement energy levels appear, which allow the excitonic transitions to be amplified by the bosonic stimulation of radiative transitions between levels in a cascade. Such a parabolic structure is a key element of the proposed bosonic cascade laser designed to generate THz radiation [26]. This concept has thus far been realized in a variety of different structures [35–37].

Stronger confinement allows one to obtain more stable quantum systems, that can operate at higher temperatures. For example, confining an exciton to a two-dimensional plane increases its ground state binding energy by a factor of four [38]. In this regard, cuprous oxide is a promising material due to large binding energies of quasiparticles already in the bulk. Indeed, bulk Cu_2O crystals have been shown to possess many sharp exciton resonances including highly excited Rydberg states [39]. The bulk exciton states, the impact of the upper subbands as well as external fields on Rydberg excitons in Cu_2O, and a variety of many-body effects have been studied in detail [40–53]. Moreover, artificially grown high-quality cuprous oxide crystals are currently being fabricated [54–60]. The grown samples of predefined size open up the possibility to confine excitons in these structures similar to QWs. The produced samples already allowed to experimentally study the radiative decay rates of Rydberg excitons in thin Cu_2O films [19] as well as the crossover from the excitonic superradiance regime to the polaritonic long-range propagation [56]. In this context, the systematic studies of Rydberg exciton states, their size-dependent properties in cuprous oxide QW-like structures become ever more important.

In this paper, we study the two-band (or hydrogenlike) model of Rydberg excitons in Cu_2O-based QWs in different regimes ranging from weak to strong confinement. We analyze the dependence of bound-state energies on a single parameter characterizing the strength of the confinement. We begin our investigation by discussing parabolic confinement along one spatial direction, for example, along the growth axis. In this case, the Kohn theorem [61,62] allows us to significantly simplify the treatment of the problem and to follow the evolution of energy levels during the crossover from weak to strong confinement. The case of weak confinement is studied numerically using an expansion of the wave function over the Coulomb-Sturmian basis. We show that in such a case, the distribution of the energy levels is determined by the degree of orientation of the corresponding wave functions over the confining direction. As the Coulomb-Sturmian basis is appropriate only for weak confinement, the evolution of the exciton energy levels during the crossover from weak to strong confinement has to be investigated by alternative numerical methods such as a finite-difference discretization [63] or a more precise B-spline expansion [64,65] of the exciton wave function. One then observes Rydberg energy levels as well as their crossings and avoided crossings during the evolution as the confinement becomes gradually stronger. Moreover, one observes that the energy levels, distributed over the value of the principal quantum number N in case of the weak confinement, change their order to a distribution over the value of the magnetic quantum number m for strong confinement.

After having understood the general picture of the evolution of the energy levels for parabolic confinement, we turn to study a rectangular QW structure. To this end, we use a two-band model of the Rydberg exciton in QW [38] with cuprous oxide material parameters [46], thus simulating the Cu_2O thin film sandwiched between vacuum or air. We disregard features of the band structure, i.e., effects of the spin-orbit split band and the nonparabolicity [38,66]. The effects of the complex valence band structure in bulk cuprous oxide have been discussed in detail before [40–42,46,47] and are thus only briefly mentioned here. We would like to point out that the overall structure of the excitonic Rydberg series can be well explained within a hydrogenlike two-band model, and only the details of the spectra require the consideration of the complete valence band structure. We use the pure Coulomb potential to observe the general structure of energy levels and further compare it with the results obtained with the Rytova-Keldysh potential [67,68], taking into account the dielectric contrast in the QW and in the barriers [69]. Our model leads to the Schrödinger equation with a Hamiltonian that produces an energy spectrum with many quantum-confinement subbands and different branches of continua. In contrast to a parabolic potential, for a rectangular confining potential one cannot separate variables, and one has to numerically solve the full three-dimensional Schrödinger equation [70]. In this regard, we expand the exciton wave function over a basis of B-splines [64,65]. Due to the large number of quantum-confined energy levels, we restrict our attention to states characterized by magnetic quantum numbers $m = 0, \pm 1$, and calculate ground and several excited energy levels below the electron-hole (*eh*) scattering threshold. The behavior of energy levels for higher magnetic quantum numbers can then be qualitatively understood from the above-mentioned model of parabolic confinement. We observe the evolution of the energy levels of Rydberg excitons during the crossover from a narrow to a wide QW. Furthermore, we show that in these limiting cases the energies can be easily calculated by expanding the wave function over quantum-confined states. The intermediate range of the QW widths, however, cannot be treated by these techniques, and one has to resort to numerical B-spline solutions. We compare our computational results with the peak positions in the photoluminescence spectrum of Cu_2O QW-like structure presented in Ref. [19].

In this paper, we focus on the bound states of *eh* pairs in a QW. In fact, a confinement along one dimension produces many quantum-confined subbands. For strong confinement, the confinement energies are large. Below each value of the sum of electron and hole confinement energies, a proper Rydberg series of *eh* energies appears. In QW systems, the *eh* bound states are located below the lowest scattering threshold, i.e., below the sum of the lowest quantum-confined energies of the disjoint electron and hole in the QW [70]. The higher-lying Rydberg series lie in the Coulomb continuum of the lower subbands, and are thus resonance states. They are characterized by additional linewidth broadening due to their finite lifetime, as the electron can scatter off the hole in the QW plane even in case of infinite QW barriers [71]. As the resonant states require a yet more elaborate treatment

[72,73], in this paper, we focus solely on the bound *eh* states, characterized by their square-integrable wave function.

The paper is organized as follows. We begin in Sec. II by setting the scene for describing Rydberg excitons in structures that provide a spatial confinement in one dimension. We then elaborate on two illustrative examples, a parabolic confinement (Sec. III) and a rectangular confinement (Sec. IV). We specify the particular $\mathrm{Cu_2O}$-based QW structure and describe numerical methods used to compute the exciton spectrum there. A detailed discussion of the obtained results is provided in Secs. III C and IV C for parabolic and rectangular confinement, respectively. Section V describes the results obtained with different dielectric constants in the QW and in the barriers. A brief discussion of the effects of the crystal environment on Rydberg excitons in QWs is presented in Sec. VI. Numerical details are given in the Appendix.

II. RYDBERG EXCITONS CONFINED IN ONE SPATIAL DIMENSION

In the two-band (or hydrogenlike) approximation [18,38], electron and hole dispersions are assumed to be parabolic, and the bound *eh* states appear solely due to the Coulomb attraction. However, the quantum confinement along one axis significantly complicates the well-known Rydberg-like series [43,46] of energy levels.

The quantum states of the *eh* pair confined in the z direction are defined by the eigenstates of the Hamiltonian

$$H = \frac{\mathbf{p}_e^2}{2m_e} + \frac{\mathbf{p}_h^2}{2m_h} - \frac{e^2}{\epsilon|\mathbf{r}_e - \mathbf{r}_h|} + V_e(z_e) + V_h(z_h), \tag{1}$$

where m_e and m_h are the effective masses of the electron and the hole in the semiconductor, respectively. The variables z_e and z_h are the coordinates along the confinement direction, whereas ρ is the distance between electron and hole in the QW plane. The confining potentials $V_e(z_e)$ and $V_h(z_h)$ break the spherical symmetry of the problem, reducing it to mere translational invariance in the QW plane. Note that we use a simple two-band model for the kinetic energy of the electron and hole in Eq. (1), which means that the effects of the complex valence band structure on Rydberg excitons in QWs are neglected. Brief remarks on these effects are given in Sec. VI.

In terms of the center-of-mass coordinate $\mathbf{R} = (m_e\mathbf{r}_e + m_h\mathbf{r}_h)/(m_e + m_h)$, and momentum $\mathbf{P} = \mathbf{p}_e + \mathbf{p}_h$, as well as the relative coordinate $\mathbf{r} = \mathbf{r}_e - \mathbf{r}_h$ and momentum $\mathbf{p} = (m_h\mathbf{p}_e - m_e\mathbf{p}_h)/(m_e + m_h)$, the *eh* Hamiltonian reads

$$H = \frac{\mathbf{P}^2}{2M} + \frac{\mathbf{p}^2}{2\mu} - \frac{e^2}{\epsilon|\mathbf{r}|} + V_e(Z + \beta z) + V_h(Z - \alpha z). \tag{2}$$

Here $M = m_e + m_h$ is the total exciton mass, $\mu = (m_e^{-1} + m_h^{-1})^{-1}$ is the reduced mass, and $\alpha = m_e/(m_e + m_h)$ and $\beta = m_h/(m_e + m_h)$ are normalized electron and hole masses, respectively.

Due to translational invariance in the QW plane, the center-of-mass motion in this plane can be separated. Furthermore, due to rotational symmetry the angular momentum component along the z direction is conserved. This implies that the unknown wave function can be written as $\psi(Z, z, \rho)\, e^{im\phi}/\sqrt{2\pi}$ where $m \in \mathbb{Z}$ is the magnetic quantum number and ϕ is the polar angle in the QW plane. For instance, the value $m = 0$ defines cylindrically symmetrical solutions. As a result, the Hamiltonian of the nontrivial *eh* motion is given by

$$\begin{aligned} H(Z, z, \rho) =& \frac{P_Z^2}{2M} + \frac{p_z^2}{2\mu} - \frac{\hbar^2}{2\mu}\left(\frac{\partial^2}{\partial\rho^2} + \frac{1}{\rho}\frac{\partial}{\partial\rho} - \frac{m^2}{\rho^2}\right) \\ &- \frac{e^2}{\epsilon\sqrt{\rho^2 + z^2}} + V_e(Z + \beta z) + V_h(Z - \alpha z). \end{aligned} \tag{3}$$

Returning to absolute z coordinates of the electron and the hole instead of the center-of-mass and relative ones (Z, z), the last equation can be written as [70]

$$\begin{aligned} H(z_e, z_h, \rho) =& -\frac{\hbar^2}{2m_e}\frac{\partial^2}{\partial z_e^2} - \frac{\hbar^2}{2m_h}\frac{\partial^2}{\partial z_h^2} \\ &- \frac{\hbar^2}{2\mu}\left(\frac{\partial^2}{\partial\rho^2} + \frac{1}{\rho}\frac{\partial}{\partial\rho} - \frac{m^2}{\rho^2}\right) \\ &- \frac{e^2}{\epsilon\sqrt{\rho^2 + (z_e - z_h)^2}} + V_e(z_e) + V_h(z_h). \end{aligned} \tag{4}$$

The energies E of the electron-hole pairs are thus the solutions of the Schrödinger equation

$$H(z_e, z_h, \rho)\psi(z_e, z_h, \rho) = E\psi(z_e, z_h, \rho). \tag{5}$$

The energies of the Rydberg exciton states can be defined with respect to the sum of the lowest quantum-confined energies $E_{e1} + E_{h1}$ of electron and hole in the confinement potentials $V_e(z_e)$ and $V_h(z_h)$, respectively. This sum specifies the lower boundary of the continuum, i.e., the lowest scattering threshold. Below $E_{e1} + E_{h1}$ there are only bound states, and above this threshold the resonant states (of the particular parity) appear. Thus the exciton binding energy is defined as

$$E_b = E_{e1} + E_{h1} - E. \tag{6}$$

III. PARABOLIC CONFINEMENT

We begin with an illustrative example of parabolic confinement over one axis that is, to a certain extent, analytically tractable in different confinement regimes and which has been realized in various semiconductor heterostructures [74–78]. We assume the confining potential to be of the form $V_{e,h}(z) = m_{e,h}\Omega^2 z^2/2$, i.e., it restricts the motion of the exciton in the z direction. With this form of the confining potential, the center-of-mass and relative motions can still be exactly separated [61,62]. That is, the wave function for the Hamiltonian (3) can be written as $\psi(Z, z, \rho) = \Psi(Z)\Phi(z, \rho)$. Here, $\Psi(Z)$ is the solution of the one-dimensional Schrödinger equation for the exciton as a whole, trapped in the harmonic potential [2]

$$\left[-\frac{\hbar^2}{2M}\frac{d^2}{dZ^2} + \frac{M\Omega^2}{2}Z^2\right]\Psi(Z) = E_Z\Psi(Z). \tag{7}$$

The function $\Phi(z,\rho)$ is, in turn, the solution of the two-dimensional equation for the relative *eh* motion,

$$\left[-\frac{\hbar^2}{2\mu}\left(\frac{\partial^2}{\partial\rho^2}+\frac{1}{\rho}\frac{\partial}{\partial\rho}-\frac{m^2}{\rho^2}\right)-\frac{e^2}{\epsilon\sqrt{\rho^2+z^2}}-\frac{\hbar^2}{2\mu}\frac{\partial^2}{\partial z^2}+\frac{\mu\Omega^2}{2}z^2\right]\Phi(z,\rho)=E_z\Phi(z,\rho). \tag{8}$$

The *eh* bound states are located below the lowest quantum confinement energy of the parabolic potential, that is, below $E_{\mu1}=\hbar\Omega/2$. Thus the binding energies (6) are defined as

$$E_b=E_{\mu1}-E_z. \tag{9}$$

Hence, the separation of variables due to parabolic confinement reduces the dimensionality of the equation of motion for the relative coordinate when compared to Eq. (5), which significantly simplifies the theoretical investigation. Numerical solution of Eq. (8) allows one to study the evolution of the energy spectrum during the crossover from the exciton in a bulk crystal (weak confinement, 3D exciton) to the exciton confined in a thin film (strong confinement, 2D exciton).

A. Weak parabolic confinement

In the case of weak parabolic confinement, the solution of Eq. (8) can be obtained by taking the weak confinement as a perturbation. In this case, the unperturbed equation is a hydrogenlike problem, and thus the expansion of the wave function is conveniently performed over hydrogenlike basis functions. To be precise, the Schrödinger equation for the hydrogenlike problem with parabolic confinement along the z axis reads

$$\left[-\frac{\hbar^2}{2\mu}\Delta-\frac{e^2}{\epsilon}\frac{1}{r}+\frac{\mu\Omega^2}{2}z^2\right]\psi(\mathbf{r})=E_z\psi(\mathbf{r}). \tag{10}$$

The parabolic potential can be expressed in terms of the radial variable and a linear combination of spherical harmonics [79] $Y_l^m(\theta,\phi)$ as

$$\frac{\mu\Omega^2}{2}(r\cos\theta)^2=\frac{\mu\Omega^2r^2}{2}\left(\sqrt{\frac{4\pi}{9}}Y_0^0(\theta,\phi)+\sqrt{\frac{16\pi}{45}}Y_2^0(\theta,\phi)\right).$$

In spherical coordinates (r,θ,φ), the three-dimensional Coulomb-Sturmian basis is convenient for expansion of the wave function as the matrix elements of the kinetic and Coulomb potential terms are known [80,81]. With radial n_r, orbital l, and magnetic m quantum numbers, the basis functions are naturally defined as

$$\Phi_{n_rlm}(r,\theta,\varphi;\lambda)=\frac{1}{r}\psi_{n_r,l}(r;\lambda)Y_l^m(\theta,\varphi), \tag{11}$$

where the Coulomb-Sturmian functions read

$$\psi_{n_r,l}(r;\lambda)=\left(\frac{n_r!}{(2l+n_r+1)!}\right)^{1/2}\mathrm{e}^{-\lambda r/2}(\lambda r)^{l+1}L_{n_r}^{2l+1}(\lambda r). \tag{12}$$

Here, $L_{n_r}^{2l+1}(\lambda r)$ are the generalized Laguerre polynomials [82] and λ is a variational parameter. Alternatively, one can redefine the functions in terms of the principal quantum number via a substitution $N=n_r+l+1$.

In this basis, the Coulomb potential is diagonal, viz.

$$\int\Phi_{n_r',l'}^{m'}(r,\theta,\varphi;\lambda)\,\frac{1}{r}\,\Phi_{n_r,l}^{m}(r,\theta,\varphi;\lambda)d\mathbf{r}=\delta_{n_rn_r'}\delta_{ll'}\delta_{mm'}.$$

The Laplace operator in the Coulomb-Sturmian basis is, in turn, tridiagonal. Correcting the typos in Ref. [80], the matrix elements of the Laplace operator are

$$\int\Phi_{n_r',l'}^{m'}(r,\theta,\varphi;\lambda)\ \Delta\ \Phi_{n_r,l}^{m}(r,\theta,\varphi;\lambda)\ d\mathbf{r}$$
$$=(-1)^{n_r+n_r'+1}\frac{\lambda^2}{4}\int\Phi_{n_r',l'}^{m'}(r,\theta,\varphi;\lambda)\ \mathbf{I}\ \Phi_{n_r,l}^{m}(r,\theta,\varphi;\lambda)d\mathbf{r}.$$

The matrix elements of the identity operator $\mathbf{I}$ are

$$\int\Phi_{n_r',l'}^{m'}(r,\theta,\varphi;\lambda)\ \mathbf{I}\ \Phi_{n_r,l}^{m}(r,\theta,\varphi;\lambda)\ d\mathbf{r}$$
$$=\delta_{ll'}\delta_{mm'}\frac{1}{\lambda}\begin{cases}2(n_r+l+1), & n_r=n_r'\\ -\sqrt{(n_r+1)(n_r+2l+2)}, & n_r=n_r'+1\end{cases}.$$

In order to calculate the matrix elements of the parabolic potential, the angular and radial dependencies are evaluated separately. The angular part gives exact expressions including the Wigner-3j symbols [79],

$$\langle Y_{l'}^{m'}|\cos^2\theta|Y_l^m\rangle$$
$$=(-1)^{m'}\sqrt{\frac{(2l'+1)(2l+1)}{4\pi}}\sqrt{\frac{4\pi}{9}}\begin{pmatrix}l' & 0 & l\\ 0 & 0 & 0\end{pmatrix}$$
$$\times\begin{pmatrix}l' & 0 & l\\ -m' & 0 & m\end{pmatrix}$$
$$+(-1)^{m'}\sqrt{\frac{5(2l'+1)(2l+1)}{4\pi}}\sqrt{\frac{16\pi}{45}}\begin{pmatrix}l' & 2 & l\\ 0 & 0 & 0\end{pmatrix}$$
$$\times\begin{pmatrix}l' & 2 & l\\ -m' & 0 & m\end{pmatrix}. \tag{13}$$

The radial part can also be computed analytically as

$$\int_0^\infty\phi_{n_r',l'}(r,\lambda)r^4\phi_{n_r,l}(r,\lambda)\ dr$$
$$=\frac{\lambda^2}{8}\sqrt{\frac{n_r!n_r'!}{(n_r+2l+1)!(n_r'+2l'+1)!}}$$
$$\times\sum_{i=0}^{n_r}\sum_{j=0}^{n_r'}(-1)^{i+j}\binom{n_r+2l+1}{n_r-i}\binom{n_r'+2l'+1}{n_r'-j}$$
$$\times\frac{(i+j+l+l'+4)!}{i!j!}. \tag{14}$$

Moreover, the sums on the rhs of Eq. (14) can be evaluated exactly as shown in Appendix of Ref. [81].

In practical calculations, when the parabolic confinement is weak (small Ω), one has to take into account basis functions with only a few quantum numbers to obtain accurate energies. For stronger confinement (larger Ω), many more basis functions are needed to achieve the same precision. As a result, despite the sparse block structure of the Hamiltonian in the Coulomb-Sturmian basis, the number of blocks is given by the maximal value of the included quantum numbers and increases as $O(l_{\max}^2 N_{\max})$. This limits the applicability of the proposed scheme and makes the solution unpractical for the strength of the confinement $A = \mu\Omega^2/2 \gtrsim 0.1\,\mathrm{Ry}/a_B^2$.

B. Strong confinement

In general, Eq. (10) determines the energies for arbitrary strength $A = \mu\Omega^2/2\,\mathrm{Ry}/a_B^2$ of the parabolic confinement. However, in case of the strong confinement (large Ω), the procedure described in the previous section is impractical. In such a case, a straightforward numerical solution of Eq. (8) is more convenient. For a wide range of Ω, it can be solved directly by the finite-difference method [71] or by an expansion of the wave function over a basis of Hermite functions [83,84] or B-splines [64]. Moreover, particularly for large Ω, one can use the adiabatic approximation, taking into account the stronger confinement along the z direction than in the QW plane (along ρ). This approximation requires, first, a determination of the one-dimensional wave functions $\phi_i(z)$ and the corresponding energy levels of the parabolically confined exciton along the z direction and, second, a solution of the coupled system of equations with the effective potential defined by the so obtained wave functions $\phi_i(z)$,

$$V_{ij}^{\mathrm{eff}}(\rho) = -\frac{e^2}{\epsilon}\int_{-\infty}^{\infty} \frac{\phi_i(z)\phi_j(z)}{\sqrt{\rho^2+z^2}}\,dz. \tag{15}$$

The adiabatic approach is accurate enough for large values of Ω, when the nondiagonal terms of the effective potential (15) are relatively small and, thus, can be treated as perturbations. This means that the motion of the exciton is, to a good approximation, two-dimensional and the energies are close to those of the 2D Coulomb series.

C. Results for parabolic confinement

In this section, we present the calculation of the Rydberg series of energy levels of excitons in parabolic quantum wells for different strengths of the confinement. The effective masses for the electron and hole in cuprous oxide, $m_e = 0.99\,m_0$ and $m_h = 0.69\,m_0$, and a dielectric constant $\epsilon = 7.5$ have been used. The variational parameter λ in Eq. (12) is taken to be 1. In our calculations, we studied only the *eh* bound states. Their energy levels are below the scattering threshold $E_{\mu 1} = \hbar\Omega/2$ of the lowest quantum confinement energy of a particle of the mass μ, see Eq. (8), in a parabolic QW along the z axis. As a result, it is convenient to characterize the calculated energy levels by their binding energies (9). Depending on the strength $A = \mu\Omega^2/2\,\mathrm{Ry}/a_B^2$ of the parabolic confinement, different methods to evaluate the energies of the exciton states have been employed.

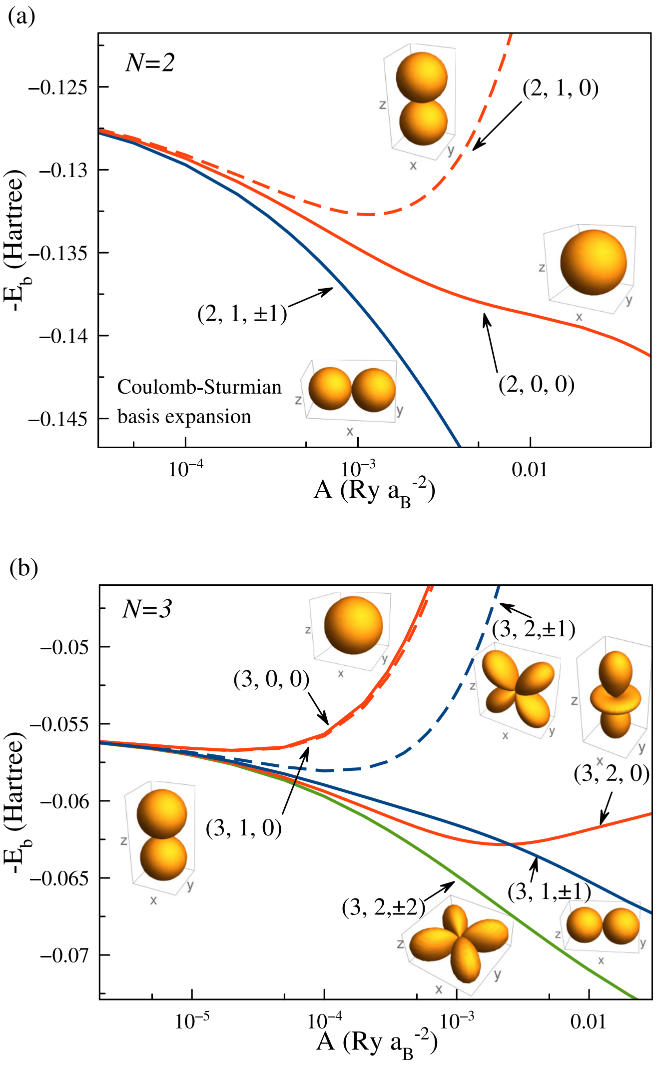

FIG. 1. Splitting of the energy levels as function of the strength of the parabolic confinement $A = \mu\Omega^2/2\,\mathrm{Ry}/a_B^2$ using Coulomb-Sturmian basis expansion. (a) Energies corresponding to principal quantum number $N = 2$ and (b) $N = 3$. The energy levels are characterized by three quantum numbers (N, l, m), where N is the principal quantum number, l is the orbital one, and m is the magnetic one. The energy levels with same $|m| \geqslant 1$ are degenerate and correspond to two different states.

For weak confinement, that is, for small A (and thus small Ω), the Coulomb-Sturmian basis (12), together with the expansion over spherical harmonics allowed us to precisely calculate the dependence of the Rydberg energies on the confinement strength as an external perturbation. In the absence of the perturbation, the Coulomb energy levels are highly degenerate. If a weak perturbation is introduced, this degeneracy is lifted. In Fig. 1, we show the gradual increase in the splitting of the energy levels with an increase in the strength, A, of the weak perturbation. Their shifts to lower or higher energies are determined mainly by the order of the alignment of the wave functions over the confining direction.

The quantum states can be characterized by three quantum numbers (N, l, m), where N is the principal quantum number, l is the orbital quantum number, and m is the magnetic one. For example, in Fig. 1, the states corresponding to principal quantum numbers $N = 2$ and 3 are shown as function of

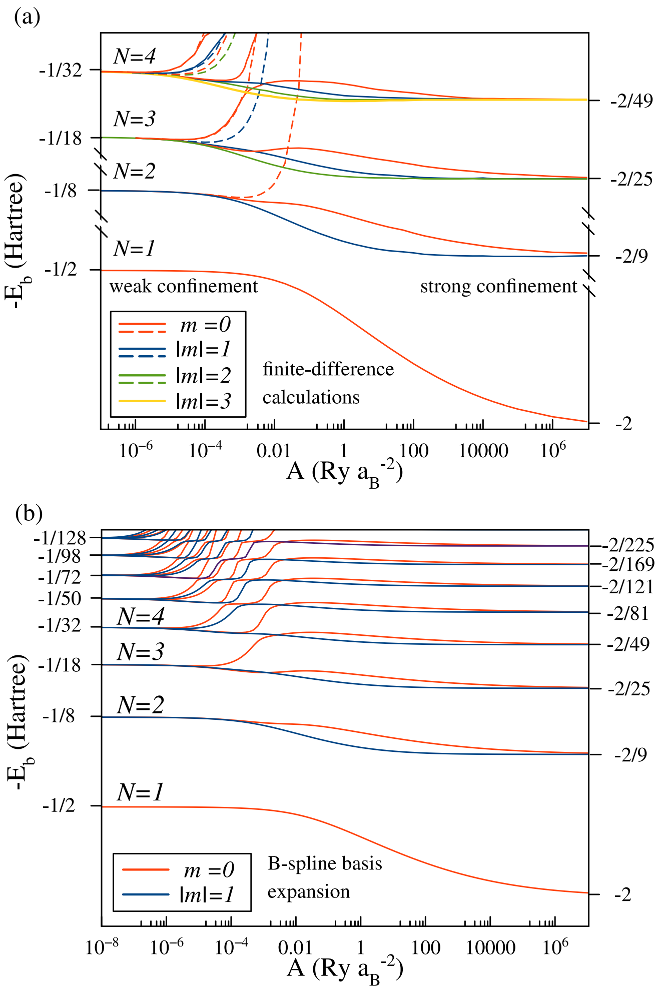

FIG. 2. The Rydberg series of exciton states depicted at the crossover from the weak to strong parabolic confinement along z. The parameter $A = \mu\Omega^2/2\,\mathrm{Ry}/a_B^2$ defines the strength of the confinement. (a) Finite-difference calculations of several of the lowest energy levels. The solid lines correspond to the bound states which remain bound for both weak and strong confinement. The dashed lines show the states whose energies diverge during the crossover to the strong confinement. (b) Results of B-spline expansion computations of the excited states. The energy levels with $|m| \leqslant 1$ are only shown for better visibility.

the confinement strength A. For $N = 2$, taking into account the degeneracy of the states $(2, 1, \pm1)$, there are just three energy levels for four bound states, see Fig. 1(a). Thus the interpretation of the results is rather straightforward [85]. One observes that the energy of the state (2,1,0) dramatically increases with growing A. The reason for this behavior is that the wave function of this state is essentially aligned along the z axis. The squeezing of the wave function induces the rapid energy increase. The wave functions of the other three states are not aligned along z, so their energies do not change drastically. This is also seen in Fig. 2(a), where the dependence of several of the lowest energy levels on a wide range of strengths A is shown. Moreover, one observes that the wave function of the state (2,0,0) is spherically symmetric, whereas the wave functions of the states $(2, 1, \pm1)$ are more aligned in the QW (xy) plane. As a result, the energy of the spherically symmetric state (2,0,0) is above those of the states $(2, 1, \pm1)$.

For a principal quantum number $N = 3$, see Fig. 1(b), the number of bound states is increased up to nine, so the interpretation of the results becomes somewhat more involved. Moreover, in this case, the distribution of states is additionally complicated by the coupling of states with the same m and with the values of l that differ by 2 [$m - m' = 0$ and $l - l' = \pm2$ in Eq. (13)]. Thus the corresponding energy levels exhibit the avoided crossings. If this coupling were absent, then again the distribution of energy levels would be mainly defined by the measure of alignment of the wave function along the z axis. The more the wave function is aligned along the confining direction, the higher the energy (lower binding energy) of the state. Therefore the state (3,1,0) would have the highest energy (lowest $|E_b|$) due to the largest z component. All other states would be located below that in energy until the lowest state $(3, 2, \pm2)$ whose wave function lies predominantly in the QW plane. However, due to their coupling, the energy levels of states with the same m and $l - l' = \pm2$ show avoided crossings. For $N = 3$, there is a coupling of the angular dependencies of the states (3,0,0) and (3,2,0). This results in a state repulsion, making the state (3,0,0) to be energetically highest. Furthermore, the states (3,2,0) and $(3, 1, \pm1)$ cross at $A \approx 0.0025\,\mathrm{Ry}/a_B^2$.

The energies of the states $(2, 1, \pm1)$, $(3, 1, \pm1)$ and $(3, 2, \pm2)$ decrease with growing strength A due to their dominant alignment along the QW plane. In fact, the energies of these states transit from weak to strong confinement. For very weak confinement (3D exciton, 3D Coulomb potential), the states are degenerate and their binding energies are $-1/2N^2$ Hartree, whereas for the limiting case of strong confinement (2D exciton, 2D Coulomb potential), their energies are $-1/2(N - 1/2)^2$ Hartree. Hence, the bound states aligned along the QW plane generally become more strongly bound as the strength A increases [38]. This is depicted in Fig. 2 where the energy levels as functions of the strength of the confinement are shown. One can see, for example, that the energy of the state $(2, 1, \pm1)$ decreases from $-1/8$ Hartree to $-2/9$ Hartree. The multiplicity of the 3D Coulomb energy level is N^2, whereas for the 2D Coulomb potential it is $2N - 1$. Therefore, for $N = 2$, we see that one of four states drastically increases its energy as the confinement growths and other three fill in the three empty vacancies in case of the strong confinement.

The Coulomb-Sturmian basis is not appropriate for a precise determination of the energies across the entire range of confinement strengths, covering both weak and strong regimes. For $N_{\max} \sim 100$ and $l_{\max} \sim 20$, the energy levels obtained using the Coulomb-Sturmian basis start to diverge at around $A \sim 0.1\,\mathrm{Ry}/a_B^2$. Therefore, for larger A, we employed the finite-difference method [63,70] to accurately calculate the lowest energy levels, see Fig. 2(a). Details are given in Appendix 1. The finite-difference approximation allowed us to precisely calculate the energy levels up to $A \sim 10^6\,\mathrm{Ry}/a_B^2$. For even stronger confinement, these results can also be obtained using the adiabatic approach, see Sec. III B, because the confinement along z dominates and the system is, to a large extent, two-dimensional.

Solving Eq. (8) by the finite-difference method allows one both to determine several of the lowest energy levels for a large range of confinement strengths, $A = 10^{-6}$–$10^{6}\ \mathrm{Ry}/a_B^2$, as well as their ordering. Although the distribution for the excited Rydberg states is rather complicated, we can draw some important conclusions from the calculated spectra. States with the same quantum numbers, that differ only by the sign of m, are degenerate. For a given principal quantum number N, the two lowest degenerate energy levels have $|m| = l = N - 1$. They remain there irrespective of the strength of the confinement, as they are mainly aligned along the QW plane and, moreover, have a minimal extent along the z axis. For weak confinement, one of the states with largest energy in a bundle is the state with $l = 1$ and $m = 0$. As it is mainly aligned along z, its energy rapidly diverges as A increases. Furthermore, for arbitrary N, the energies of states with $|m| = l - 1$ diverge. The spherical harmonics of these states are proportional to z/r and thus the corresponding matrix element of the parabolic potential is positive and grows drastically with increasing A.

Generally, the quantum confinement leads to an increase of the binding energy [38]. However, one can see that instead some states increase their energies (diminish E_b) by crossing over higher-lying states with growing confinement, see Fig. 2(b). During the crossover from weak to strong confinement, the energy levels for fixed N are stacked above the lowest states $(N, N-1, \pm(N-1))$ with decreasing magnetic quantum number m. This can be seen in Fig. 2(a) where for $N = 4$, the energy levels of the bound states are ordered from bottom to top of the bundle as $|m| = 3, 2, 1, 0$.

Although the finite-difference method allows for a precise determination of lower-lying energy levels, it is less appropriate for the calculation of high-lying Rydberg exciton energy levels. The wave functions of the Rydberg states are significantly spatially extended and require using fine grids over a broad calculation domain. The B-spline basis expansion [65] of the wave function in Eq. (8) makes it possible to overcome these technical issues and to accurately estimate many excited energy levels for a wide range of confinement strengths. We used B-splines of fifth order to represent the wave function, that led to the generalized eigenvalue problem which was solved by the QR algorithm [86]. The details on the B-spline calculations are given in Appendix 2.

In Fig. 2(b), we show the results of the B-spline calculations of the energy levels for magnetic quantum numbers $|m| = 0, 1$. One observes a crossover from weak to strong confinement as well as crossings and avoided crossings of different excited energy levels. As already mentioned, for weak confinement the energy levels are ordered according to the energies of the 3D Coulomb potential, $-1/2N^2$, whereas for strong confinement they are governed by the 2D Coulomb potential $-1/2(N - 1/2)^2$. In the intermediate region, for a given N, the splitting of energy levels into bundles with different values of $|m|$ occurs.

The comparison of the exciton energies obtained by the B-spline expansion method and by the limiting expansions in weak and strong confinement regimes is shown in Fig. 3. The accurate B-spline solution is represented by the solid curves, whereas the energies calculated using the Coulomb-Sturmian and the adiabatic expansion methods are shown by dashed curves. One can see that, although the limiting expansions are appropriate in the domain close to the corresponding limits, they are inaccurate for the whole studied range of confinement strengths. Interestingly, deviations produced by the limiting models for energy levels with $m > 0$ are noticeably smaller than for ones with $m = 0$. They originate from different properties of the solutions of Eq. (8) as $\rho \to 0$. Along the ρ direction, the eigenfunctions of Eq. (8) with $m > 0$ vanish as $\rho \to 0$, whereas the solution for $m = 0$ converges to a maximal constant value as $\rho \to 0$. The latter leads to a significant contribution to the potential term in Eq. (15) in the interaction domain near $\rho = 0$. For $m > 0$, as the solutions vanish as $\rho \to 0$, such contributions are much smaller and the deviations produced by the adiabatic and Coulomb-Sturmian expansions are reduced.

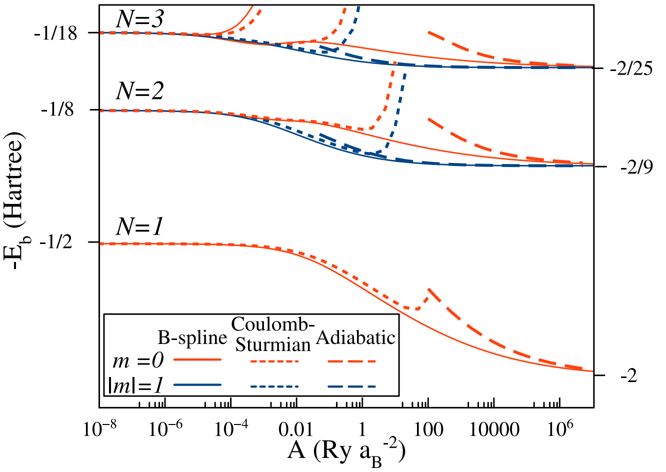

FIG. 3. Exciton energies calculated by the B-spline expansion method (solid curves) in comparison with the ones obtained using the Coulomb-Sturmian (fine-dashed curves) and the adiabatic expansions (coarse-dashed curves).

IV. RECTANGULAR CONFINEMENT

In this section, we consider a rectangular confining potential

$$V_{e,h}(z_{e,h}) = \begin{cases} 0 & \text{if } |z_{e,h}| < L/2 \\ \infty & \text{if } |z_{e,h}| \geqslant L/2 \end{cases}, \tag{16}$$

where L is the QW width. In the case of a rectangular QW confinement, the center-of-mass and relative coordinates along the confinement direction (z axis) in Eq. (5) can no longer be separated. Therefore, in contrast to the previous section where the two-dimensional Schrödinger equation has been studied, here the complete three-dimensional Eq. (3) needs to be solved. Nonetheless, we can adopt some of the approaches from the previous section. We will treat the weak confinement as perturbation, with the three-dimensional Coulomb wave functions being the eigenfunctions of the unperturbed problem. Vice versa, the 3D Coulomb interaction will be considered as a perturbation in the case of strong confinement. For both approaches, we solve the problem by expanding the three-dimensional wave function into the respective tailored basis functions. As a benchmark for comparison of the weak and strong confinement approaches, we will compare the results with those using the B-spline basis expansion. The B-spline basis is appropriate for computing the Rydberg energy levels for the whole range of studied QW widths, covering both weak and strong confinement regimes as well as the intermediate region, where the perturbative approaches are inaccurate.

A. Weak confinement

It has been suggested [38] to treat the weak confinement of excitons by confining the motion of the exciton as a whole in terms of the center-of-mass coordinate Z, while the relative motion of electron and hole is not influenced by the confinement. Then, the nontrivial radial part of the wave function can be represented as an infinite sum [70]

$$\psi(Z, z, \rho) = \sum_{k,Nl} c_{kNl}\, \phi_k(Z)\, \psi_{Nl}(\sqrt{\rho^2 + z^2}; \lambda), \tag{17}$$

where

$$\phi_k(Z) = \sqrt{\frac{2}{L}} \begin{cases} \cos(\pi k Z/L) & \text{if } k = 1, 3, 5, \dots \\ \sin(\pi k Z/L) & \text{if } k = 2, 4, 6, \dots \end{cases}$$

are the confinement states of a QW with infinite barriers. The relative motion of electron and hole is governed by the 3D Coulomb potential. As a result, $\psi_{Nl}(r; \lambda)$ are the Coulomb-Sturmian functions (12), which have been introduced for weak parabolic confinement.

We use the terms of the expansion (17) to calculate the matrix elements of the exciton Hamiltonian $H(Z, z, \rho)$, see Eq. (3), i.e., including both the confinement of center-of-mass and the relative motion:

$$\int \psi_{N'l'}(\rho, z; \lambda)\, \phi_{k'}(Z)\, H(Z, z, \rho)\, \psi_{Nl}(\rho, z; \lambda)\, \phi_k(Z)\, dZ\, dz\, d\rho. \tag{18}$$

The zero boundary conditions are defined by the barriers of the confinement potentials $V_{e,h}(z_{e,h})$. As the confinement potentials depend both on z and Z, the boundary conditions cannot be fulfilled by the basis wave functions (17), which are separable in z and Z. In analogy to the strong parabolic confinement, we make use of the adiabatic approach to obtain an effective Z-dependent potential by integrating over the relative coordinates (ρ, z). Hereby, for each value of Z the domain of integration over the z coordinate is defined by the confinement potentials. As a result, the full integration domain in the (Z, z) plane is reduced to a rhombic-like region [70]. Because of such an integration domain, one can no longer employ the recurrence relations of the Coulomb-Sturmian functions, but instead one has to numerically integrate them over z and ρ.

B. Strong confinement

For strong confinement, one can assume a separate quantization of the electron and the hole motion along the confinement axis, leading to the confinement states $\phi_{i,j}(z_{e,h})$ [38]. Moreover, the in-plane properties of the wave function are, in turn, mainly determined by the 2D Coulomb potential. As a result, the exciton wave function can be expanded as

$$\psi(\rho, \varphi, z_e, z_h; \lambda) = \sum_{ijNm} c_{ijNm}\, \phi_i(z_e)\, \phi_j(z_h)\, \Phi_{Nm}(\rho, \varphi; \lambda). \tag{19}$$

We introduce the 2D Coulomb-Sturmian functions as [87]

$$\Phi_{Nm}(\rho, \varphi; \lambda) = \frac{1}{\sqrt{\rho}}\, \phi_{Nm}(\rho; \lambda)\, \frac{e^{im\varphi}}{\sqrt{2\pi}}, \tag{20}$$

where N and m are the principal and magnetic quantum numbers, respectively, and

$$\phi_{Nm}(\rho; \lambda) = \sqrt{\frac{(N - |m| - 1)!}{(N + |m| - 1)!}}\, e^{-\rho/\lambda} \left(\frac{2\rho}{\lambda}\right)^{|m|+1/2} \times L^{2|m|}_{N-|m|-1}\left(\frac{2\rho}{\lambda}\right).$$

Similar to the case of weak parabolic confinement, we expand the exciton wave function in the basis (19) and find the tridiagonal matrix of the (in-plane) Laplace operator as

$$\begin{aligned} &\iint \Phi_{N'm'}(\boldsymbol{\rho}; \lambda)\, \triangle_{\boldsymbol{\rho}}\, \Phi_{Nm}(\boldsymbol{\rho}; \lambda) \mathrm{d}\boldsymbol{\rho} \\ &= \frac{\delta_{m'm}}{\lambda} \Bigg[-\left(N - \frac{1}{2}\right) \delta_{N'N} - \frac{1}{2} \Big(\sqrt{(N - m)(N + m)}\, \delta_{N'(N+1)} \\ &\quad + \sqrt{(N + m - 1)(N - m - 1)}\, \delta_{N'(N-1)} \Big) \Bigg], \end{aligned}$$

as well as of the identity operator

$$\begin{aligned} &\iint \Phi_{N'm'}(\boldsymbol{\rho}; \lambda) \Phi_{Nm}(\boldsymbol{\rho}; \lambda) \mathrm{d}\boldsymbol{\rho} \\ &= \delta_{m'm}\, \lambda \Bigg[\left(N - \frac{1}{2}\right) \delta_{N'N} \\ &\quad - \frac{1}{2} \Big(\sqrt{(N - m)(N + m)}\, \delta_{N'(N+1)} \\ &\quad + \sqrt{(N + m - 1)(N - m - 1)}\, \delta_{N'(N-1)} \Big) \Bigg]. \end{aligned}$$

The basis is diagonal with respect to the 2D Coulomb potential

$$\iint \Phi_{N'm'}(\boldsymbol{\rho}; \lambda) \frac{1}{\rho} \Phi_{Nm}(\boldsymbol{\rho}; \lambda) \mathrm{d}\boldsymbol{\rho} = \delta_{N'N}\, \delta_{m'm}. \tag{21}$$

This allows us to treat the difference to the 3D Coulomb potential as a perturbation

$$\begin{aligned} &\iint \Phi_{N'm'}(\boldsymbol{\rho}; \lambda) \left(\frac{1}{\sqrt{\rho^2 + (z_e - z_h)^2}} - \frac{1}{\rho} \right) \Phi_{Nm}(\boldsymbol{\rho}; \lambda) \mathrm{d}\boldsymbol{\rho} \\ &= V^{N'N}_{\text{perturb}}(z_e, z_h). \end{aligned} \tag{22}$$

Further integration of the QW confinement functions $\phi_{i,j}(z_{e,h})$ over z_e and z_h is straightforward, however, for the perturbation potential (22) this can only be done numerically.

C. Results for rectangular confinement

Using the material parameters for the electron and the hole in cuprous oxide from Sec. III C, the Rydberg energy and the

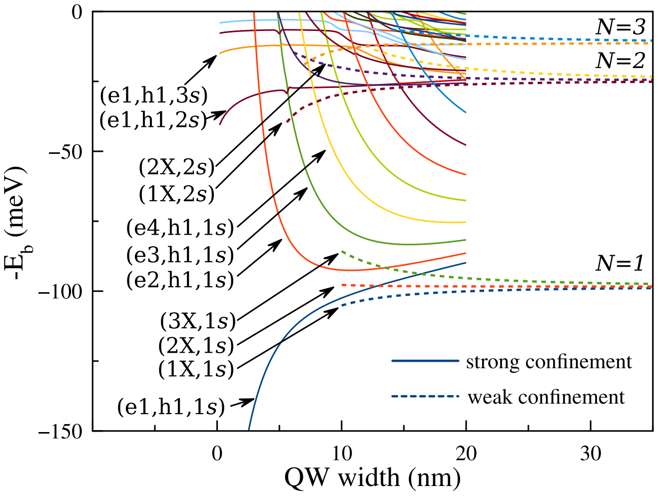

FIG. 4. Exciton energy levels as a function of the QW width for $m = 0$. The solid curves show the energy levels obtained using the expansion over 2D Coulomb-Sturmian basis (strong-confinement expansion), for the dashed ones, we use the 3D basis (weak-confinement expansion). For clarity, higher confinement states (kX, Ns) are only partly shown. Selected classified energy levels are denoted.

Bohr radius of the lowest hydrogenlike exciton state in a bulk crystal are

$$\mathrm{Ry} = \frac{\mu e^4}{2\epsilon^2\hbar^2} = 98.35\ \mathrm{meV}, \quad a_B = \frac{\epsilon\hbar^2}{\mu e^2} = 0.976\ \mathrm{nm}.$$

The latter value means that the Bohr radius of the exciton ground state is around 1 nm. Thus, for this state QW thicknesses L (or sizes of the crystal) of the order of 10 nm and wider can be considered as a model of wide QWs. Such a model assumes that the Coulomb potential dominates, whereas quantization due to QW barriers can be treated as a small perturbation. As a result, for such QW widths the representation (17) is justified.

In our study, we have computed the binding energies of the exciton states in the weak and strong confinement regimes using the expansions (17) and (19), respectively. The calculated binding energies are presented in Fig. 4 in the respective limits of wide and narrow quantum wells. In these limits, both numerical methods show good convergence: the calculated Rydberg energy series correspond to the models of 3D Coulomb and 2D Coulomb confinement. However, the convergence becomes worse if one moves away from the limiting regimes. For example, if one considers the model of a narrow QW (strong-confinement expansion), and starts to gradually increase L, then the calculated results start to gradually diverge. One can see in the figure that the energies of the strong-confinement expansion do not asymptotically converge to the Rydberg energies as $L \to \infty$. Instead of approaching the constant value, the ground and excited state energies diverge. By contrast, the weak-confinement basis expansion (17) allows one to precisely calculate the exciton energies over a broad range of QW widths, when $L \gg a_B$. The calculated energies are shown in Fig. 4 by dashed curves. One can see the precisely obtained several lowest energies of the Rydberg series $N = 1$, 2, and 3. For smaller L, this expansion gives inaccurate results.

The strong-confinement expansion (19) makes it possible to directly assign quantum numbers to the calculated energy levels. In the simplest case, our calculations are restricted to cylindrically symmetric solutions, $m = 0$. Therefore we can use three quantum numbers (ei, hj, Ns) that refer to the ith electron quantum-confinement state, the jth hole quantum-confinement state and the 2D Coulomb principal quantum number N. Similarly, for the weak-confinement expansion (17) it is convenient to introduce two quantum numbers: k is for the kth quantized state of the exciton as a whole over the z axis, and N is for the 3D Coulomb principal quantum number. They are collected in the doublet (kX, Ns), where X stands for the exciton. It is worth noting that, as resulting from Eq. (17), in general different orbital quantum numbers are allowed, although here we restrict ourselves to the simplest case of $l = 0$. The assignments are exact in the corresponding limiting cases of strong and weak confinement. However, when leaving the respective limits, they become approximate due to a mixing of the basis states.

The assignment of the curves is illustrated in Fig. 4. As a function of the QW width, the curves can be roughly divided into two groups: those which are approximately constant in energy over the whole range of QW widths, and those with strongly decreasing energies. The first group comprise states corresponding to the lowest Rydberg series, i.e., the exciton states below the lowest scattering threshold $E_{e1} + E_{h1}$ [70]. They are best seen by the dashed curves and the horizontal solid ones. These states, from bottom to top, are characterized by a triplet of quantum numbers $(e1, h1, Ns)$ with increasing $N = 1, 2, \ldots$ characterizing the energies in the Rydberg series. They accumulate around zero binding energy, which corresponds to the above-mentioned lowest scattering threshold.

The second group of levels comprise of those with decreasing energies as L grows and which, moreover, converge to the energies of the first group as $L \to \infty$. The energies of the second group originate from the excited electron and hole quantum-confinement states $E_{ei,hj}$, where either $i > 1$ or $j > 1$. These one-particle states form the subbands in the energy spectrum [70]. Each subband has a scattering threshold, $E_{ei} + E_{hj}$, producing a certain branch of the continuum. Below each scattering threshold there is a proper Rydberg series of energy levels. For small QW widths, the quantum confinement is strong, and the energy separation between one-particle states is large. Therefore, for small L, the upper subbands lie high in the continuum, far above the lowest scattering threshold $E_{e1} + E_{h1}$ [70]. These eh states are resonant (or quasibound) ones. As a result, there is only one, namely the lowest, Rydberg series of 2D Coulomb-like eh bound states in the spectrum for small QW widths. As L increases, the strength of the confinement is gradually reduced and the energy distance between quantum-confinement states decreases. The upper subbands gradually decrease in energy causing a penetration of the electron-hole resonant states below the threshold $E_{e1} + E_{h1}$, making them bound. As a result, with increasing L, more eh bound states, exciton states, appear in the spectrum. For cuprous oxide $m_e > m_h$, hence the lowest states which appear in the discrete part of the spectrum are those with the excited electron eigenmodes ei, $i = 2, 3, \ldots$

In analogy to the parabolic confinement, we also see in Fig. 4 that the alignment of the exciton states, obtained from the expansion for the weak confinement, along the z axis determines their order with respect to energy. This can be seen, for example, by tracing the lowest states which converge to the $N = 1$ or $N = 2$ Rydberg energy levels. As L decreases, the lowest state $(1X, 1s)$ turns into the $(e1, h1, 1s)$ state. Similar to the one-particle states in the QW, the second lowest state, $(2X, 1s)$ is above $(1X, 1s)$ due to its more spread-out wave function over the confinement direction.

The assignment becomes particularly complicated for the higher-lying states due to the coupling with a large number of confinement states. Moreover, even for the lower energy levels, the strong- and weak-confinement expansion calculations poorly match in the intermediate region of QW widths. To reliably calculate the energies in the intermediate region between the strong and weak confinement, as well as in order to correctly identify the energy levels of the higher states, a precise numerical method is required.

Similar to the previous sections of parabolic confinement, the energy levels of the exciton in the rectangular QW can be calculated using the finite-difference approach [63,70]. However, an accurate solution of the three-dimensional Eq. (4) by finite differences is feasible only for a few low eigenstates. For a precise determination of many Rydberg energies we applied the more powerful B-spline expansion method [64]. The numerical details of this method are given in Appendix 2.

We calculated the energy levels of the exciton in Cu_2O-based QWs of various widths ranging from 0.2 nm until 50 nm, which includes the crossover from the limits of narrow QWs, when $L \ll a_B$, to that of wide QWs, when $L \gg a_B$. For better visibility, in Fig. 5, we show the obtained binding energies of different exciton states as function of the QW width for $L < 30$ nm. The binding energies are presented with respect to the lower boundary of the continuum, $E_{e1} + E_{h1}$, which is conventionally denoted by the zero energy level. In Fig. 5, panel (a) shows all calculated energy levels, whereas panel (b) presents the enlarged domain of the Rydberg energy levels (Ns, $N = 2, \ldots, 9$) and the excited quantum-confinement states to highlight the crossings and avoided crossings.

The calculated *eh* bound states in Fig. 5 were subject to the same classification, (ei, hj, Ns), based on the types of their in-plane relative and quantum-confinement motions as in Fig. 4. Such a classification is exact for narrow QWs. For wider QWs, it is only approximate. It represents the dominant pure state $|ei, hj, Ns\rangle$ of the exciton in a very narrow QW, inherent in the calculated state for a given L.

Figure 5(b) shows the exciton Rydberg energy levels (2s–9s-like states), their evolution with increase of the QW width and the crossings/avoided crossings with other identified quantum-confinement energy levels. If there are two states of the same symmetry of the quantum-confinement eigenmodes, for example $(e3, h1, 1s)$ and $(e1, h1, 2s)$, then the corresponding energy levels show an avoided crossing. If there are states of different symmetry, then their energies cross, see for example the states $(e1, h1, 2s)$ and $(e2, h1, 1s)$.

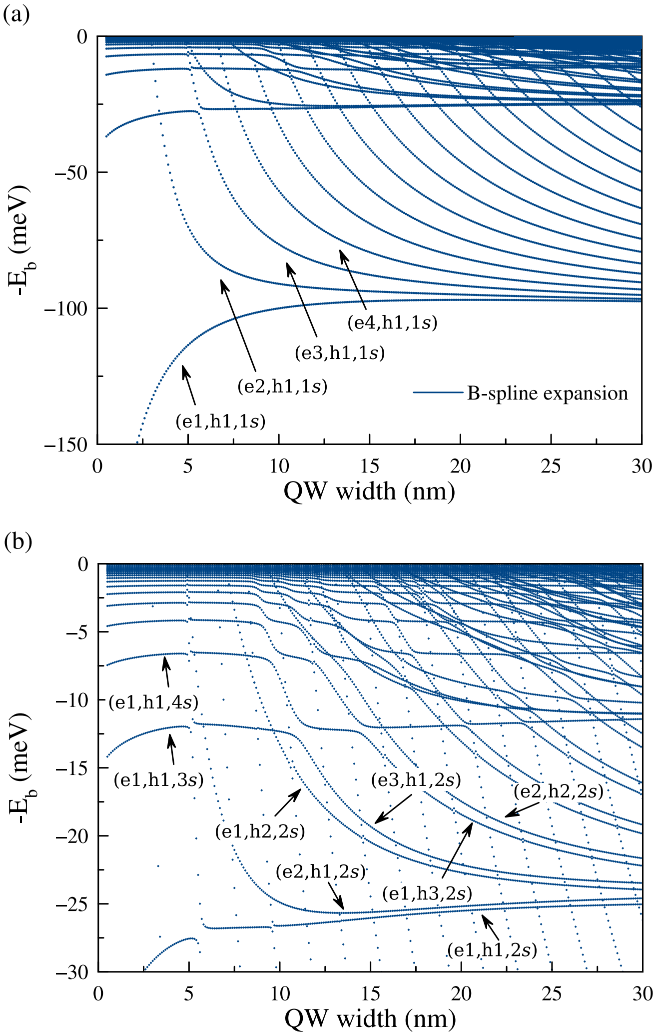

FIG. 5. (a) All calculated energy levels of the exciton in a Cu_2O QW as a function of the QW width for $m = 0$. The method of the B-spline expansion of the wave function is applied. The energy levels are labeled as (ei, hj, Ns), where i and j are the indices of the electron and hole quantum-confinement states, and N is the principal quantum number of the s-like Coulomb state. (b) Close-up of selected Rydberg energy levels. At this scale, the energy levels of states $(e2, h1, 1s)$ and $(e3, h1, 1s)$ as well as other quantum-confinement ones at panel (a) look like almost vertical series lines.

A comparison of the B-spline numerical results with limiting model data is shown in Fig. 6. Panel (a) demonstrates the data obtained using the B-spline expansion together with the results of the strong-confinement expansion calculation. Panel (b), in turn, shows the numerical data compared to the energies from the weak-confinement approximation of the exciton wave function. One can see that the strong- and weak-confinement approximations work well in the corresponding limits of narrow and wide QWs, respectively. The strong-confinement approximation allows one to precisely determine the series of Rydberg energy levels for narrow QWs, i.e., for the 2D Coulomb potential $-\rho^{-1}$. For wider QWs, when the *eh* motion is no longer two-dimensional, this approximation is inaccurate. Instead, the weak-confinement approximation is precise. One can see the improving agreement between lowest quantum-confinement states as L grows. The upper quantum-confinement energy levels show less precise correspondence due to inaccuracy in the B-spline approximation of highly oscillating wave functions of the upper QW confined states.

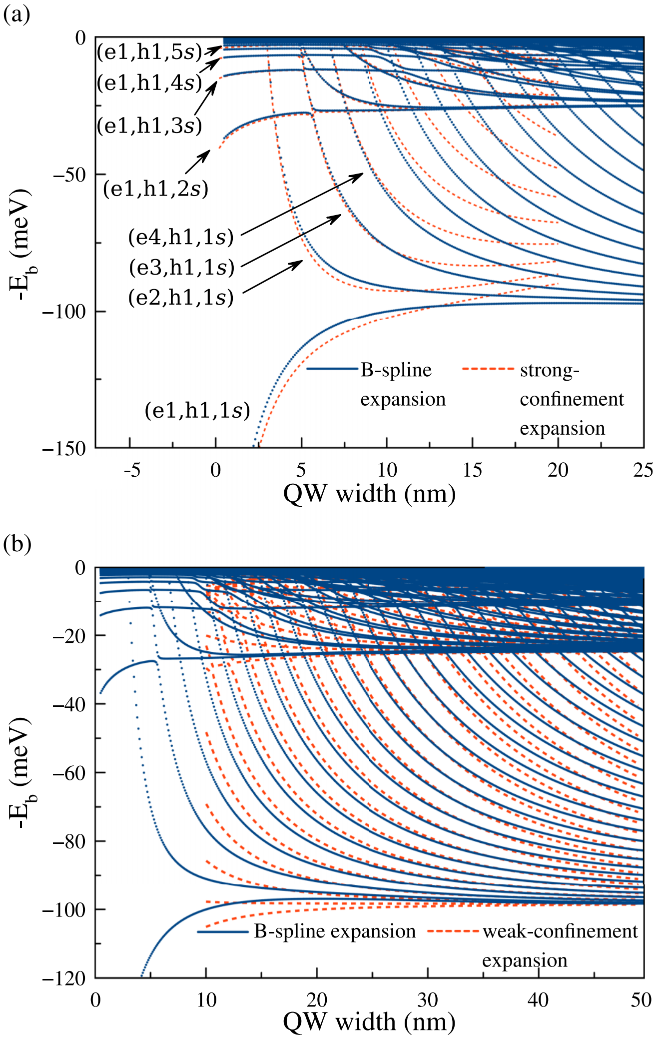

FIG. 6. Comparison of (a) the strong-confinement and (b) the weak-confinement expansion calculations with the data obtained from B-spline expansion. For simplicity, only s-like states are shown.

Increase of the size of the B-spline basis gives an improvement in the accuracy.

In order to compare our two-band model and the energies it produces with the experimental measurements [19,56], we calculated energy levels of the exciton states with $|m| = 1$ as a function of the QW width, see Fig. 7. In contrast to the case of cylindrically symmetrical states, with $m = 0$, which we call s-like states, those with $|m| = 1$ can be attributed to p-like states. The numerical method allowed us to obtained the energies up to at least the $10p$ Rydberg level. Similar to the s-like energies, among p-like states there are many quantum-confinement energy levels as well as their crossings and avoided crossings. However, despite the general similarity of the dependencies of s-like and p-like energy levels on the QW width, the detailed comparison reveals noticeable discrepancies of the states of two different kinds. These differences are especially pronounced for energy levels of the lowest quantum-confinement subband, $(e1, h1, Ns)$ and $(e1, h1, Np)$, with $N = 2, \dots, 5$ for the QW width $L < 15$ nm.

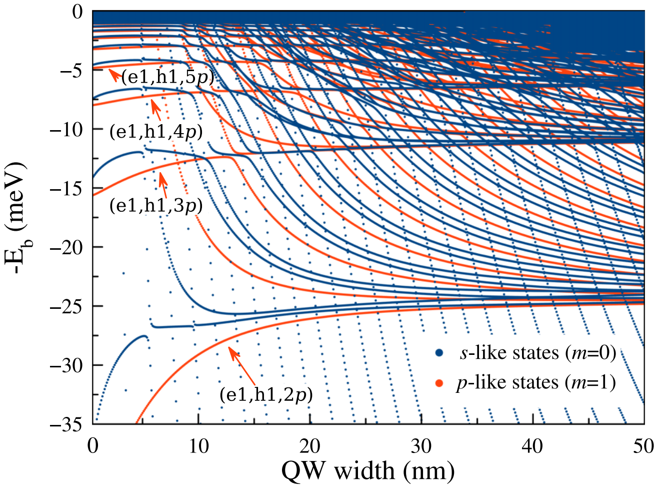

FIG. 7. Calculated p-like ($m = 1$) energy levels of the exciton in a Cu_2O QW compared to the s-like ones ($m = 0$). The method of the B-spline expansion of the wave function is applied. The energy levels are labeled as (ei, hj, Np), where i and j are the indices of the electron and hole quantum-confinement states, and N is the principal quantum number.

In complete analogy to the parabolic confinement, the s- and p-like states degenerate only in the limiting cases of strong and weak confinement. For the intermediate region of $0 < L < \infty$ the energies of p-like states are lower than the corresponding s-like ones. These discrepancies originate from the QW barriers, which break the exact spherical symmetry of the hydrogenlike exciton, leaving behind only a cylindrical symmetry. This leads to different energies of the states with different absolute values of the magnetic quantum numbers (and also with different values of orbital ones) for the same principal quantum numbers.

Our energy levels of the p-like exciton states can be compared to the photoluminescence spectra measured for different QW widths, see Ref. [19]. The peak positions of $2p$-, $3p$-, and $4p$-like exciton states of the measured spectra well agree with the corresponding calculated energy levels. In particular, one can see in Ref. [19], Fig. 2(a), that the energy differences between $3p$- and $2p$-like as well as between $4p$- and $3p$-like states are 14 and 5 meV, respectively. Very similar energy differences are observed in Fig. 7 for QW width $L \sim 50$ nm, which means a good agreement between experiment and theory.

V. ELECTROSTATIC EFFECT OF THE BARRIER MATERIAL ON THE ELECTRON-HOLE INTERACTION

The quantum confinement is the main effect determining the energy levels. However, it is not the only effect. Facets of the heterojunction of the cuprous oxide crystal embedded into air or in a substrate (sapphire or quartz) are characterized by different dielectric constants. In order to describe an experimental setup as in Ref. [19] in which a thin film of Cu_2O is sandwiched by a substrate material, we consider an effect of the dielectric contrast in the film and in the substrate to the energy levels of the Rydberg exciton. The heterostructure with different dielectric permittivities leads to different rates of charge screening and thus to a distortion of the Coulomb interaction between charge carriers. This is especially important for narrow structures in which the electrostatic field is mainly concentrated in the substrate, but not in the film [88,89]. The electron-hole interactions in a heterostructure with dielectric contrast are rigorously described by the Rytova-Keldysh potential [67,68]. It defines the infinite series of the Coulomb-like interaction potentials between the given charge and the fictional image charges.

For an electron and a hole in a structure with the dielectric constant ϵ_{QW} in the QW and ϵ_{b} in the barrier, the Rytova-Keldysh potential is given by

$$\begin{aligned} V(\vec{\rho}, z_e, z_h) &= -\frac{4\pi e^2}{\epsilon_{\text{QW}}} \int \frac{d^2k}{(2\pi)^2} e^{i\mathbf{k}\vec{\rho}} \\ &\quad \times \frac{\cosh\left[k(L/2 - z_e) + \eta\right] \cosh\left[k(L/2 + z_h) + \eta\right]}{k \sinh\left[kL + 2\eta\right]}, \end{aligned} \tag{23}$$

where $\eta = \frac{1}{2}\ln\frac{\epsilon_{\text{QW}}+\epsilon_{\text{b}}}{\epsilon_{\text{QW}}-\epsilon_{\text{b}}}$. When using a series expansion for the denominator, i.e.,

$$\frac{1}{\sinh x} = 2\sum_{n=0}^{\infty} \mathrm{e}^{-(2n+1)x} \tag{24}$$

for $x > 0$, the Fourier integrals can be solved analytically resulting in the potential

$$V(\rho, z_e, z_h) = -\frac{e^2}{\epsilon_{\text{QW}}} \sum_{n=-\infty}^{+\infty} \frac{\gamma^{|n|}}{\sqrt{\rho^2 + \left(z_e - z_h^{(n)}\right)^2}}, \tag{25}$$

with $\gamma = \frac{\epsilon_{\text{QW}}-\epsilon_{\text{b}}}{\epsilon_{\text{QW}}+\epsilon_{\text{b}}}$. Here, $z_h^{(n)} = (-1)^n L - z_h^{(n-1)}$ with $z_h^{(0)} = z_h$ are the z positions of introduced image charges of the hole after $|n|$ alternating mirror reflections at the two barrier surfaces at $z = \pm L/2$ in complementary order for $n \gtrless 0$. Note that the image charges are located on a line perpendicular to the barrier planes of the QW and decrease exponentially with the number $|n|$ of the reflections.

In the 2D limit, the potential (23) is reduced to the effective potential, given by the difference of the Struve function $S(x)$ and the Bessel function of the second kind $Y_0(x)$ as

$$V_{\text{eff}}(\rho) = -\frac{\pi e^2}{L\epsilon_{\text{QW}}}\left[S(\rho/\rho_0) - Y_0(\rho/\rho_0)\right].$$

Here $\rho_0 = L\epsilon_{\text{QW}}/(2\epsilon_{\text{b}})$ is the parameter defining the scale of the interactions. This potential has a singular behavior $V_{\text{eff}}(\rho) \sim -\ln\rho$ as $\rho \to 0$ and the Coulomb-like asymptotic form $V_{\text{eff}}(\rho) \sim -\rho^{-1}$ as $\rho \to \infty$ [90,91].

It is worth noting that the dimensional reduction also introduces a similar logarithmic divergence of the effective 2D potential of the pure Coulomb interaction [92]. The point is that the averaging of the Coulomb potential over the quantum confinement wave functions results in the effective 2D interactions in such a way that it behaves as $\sim -\ln\rho$ as the 2D radius $\rho \to 0$. The direct B-spline-expansion solution of the 3D Schrödinger equation is equivalent to the method of the solution by averaging of the problem over the z direction and then solving the effective equation for the in-plane motion (over ρ) with the potential (15). Thus, during a crossover to the 2D geometry, our effective 2D potential simulates a logarithmic divergence as $\rho \to 0$.

As a result, the effect of the dielectric contrast at the heterojunction does not introduce new singularities of the potential. Therefore the general structure of the Rydberg and quantum-confinement energy levels should still hold and only the details change. The strongest effect of the Rytova-Keldysh potential occurs for narrow QWs. As the strength of the confinement depends on the quantum number of a given state, the Rytova-Keldysh potential can also noticeably change the Rydberg states of the confined exciton for $L \gg a_B$.

To study this issue, we calculated the energy spectrum of the *eh* bound states with the interactions described by the Rytova-Keldysh potential. We used the dielectric constant $\epsilon_{\text{QW}} = 7.5$ in QW and $\epsilon_{\text{b}} = 3$ in the barrier. The latter is a typical value for a sapphire or quartz substrate [93]. With these values the image charge $e\gamma^{|n|}$ in Eq. (25) is reduced by about three orders of magnitude after eight mirror reflections, which guarantees the fast convergence of the potential. A comparison of the results with the Rytova-Keldysh and the Coulomb potential is shown in Fig. 8. One can see that, generally, up to an additive constant, the structure of energy levels is similar for both potentials. Nevertheless, one observes that the dielectric contrast with $\epsilon_{\text{b}} < \epsilon_{\text{QW}}$ shifts the energies downward, hence the ground and excited states become more localized, and eventually more bound states appear in the spectrum. This means that, due to the lower ϵ_{b} in the substrate, the *eh* interaction becomes stronger. The penetration of the electrostatic field in the barrier material is increased due to the factor $1/\epsilon_{\text{b}}$, compared to $1/\epsilon_{\text{QW}}$ in the QW. This also leads to larger avoided crossings. Moreover, the region where the avoided crossings take place is naturally a transition region from weak to strong confinement. For the Rytova-Keldysh potential, this region, as a whole, is shifted to the lower QW widths. This is again the result of the increased *eh* interaction in the barrier material, compared to the case when $\epsilon_{\text{b}} = \epsilon_{\text{QW}}$. The upper states with, for example, quantum numbers $(e1, h1, 4s)$ and Rydberg exciton states with higher principal quantum number in Fig. 8(b) are clearly in the transition region or in the strong confinement region for L up to 30 nm.

One can also see from the figure that some states degenerate more rapidly as $L \to \infty$ with the Rytova-Keldysh interactions than with the Coulomb potential. This takes place, for example, for the $(e1, h1, 1s)$ and $(e2, h1, 1s)$ states. This is a direct consequence of the shifted transition region. The degenerate energy levels at smaller QW widths mean that, for the Rytova-Keldysh potential, the relatively weaker confinement appears at smaller L, due to the relative increase of the *eh* interactions (when $\epsilon_{\text{b}} < \epsilon_{\text{QW}}$), than in the case of the pure Coulomb potential.

A comparison of the Rytova-Keldysh results with the photoluminescence data given in Ref. [19] shows reproducing the same energy differences as the Coulomb interactions do. The point is that both the calculated p-like energy levels for the weak confinement asymptotically as $L \to \infty$ converge to the same values. The measurements were done for a thickness $L \sim 100$ nm and larger for which our calculations with both the potentials produce the same energy differences.

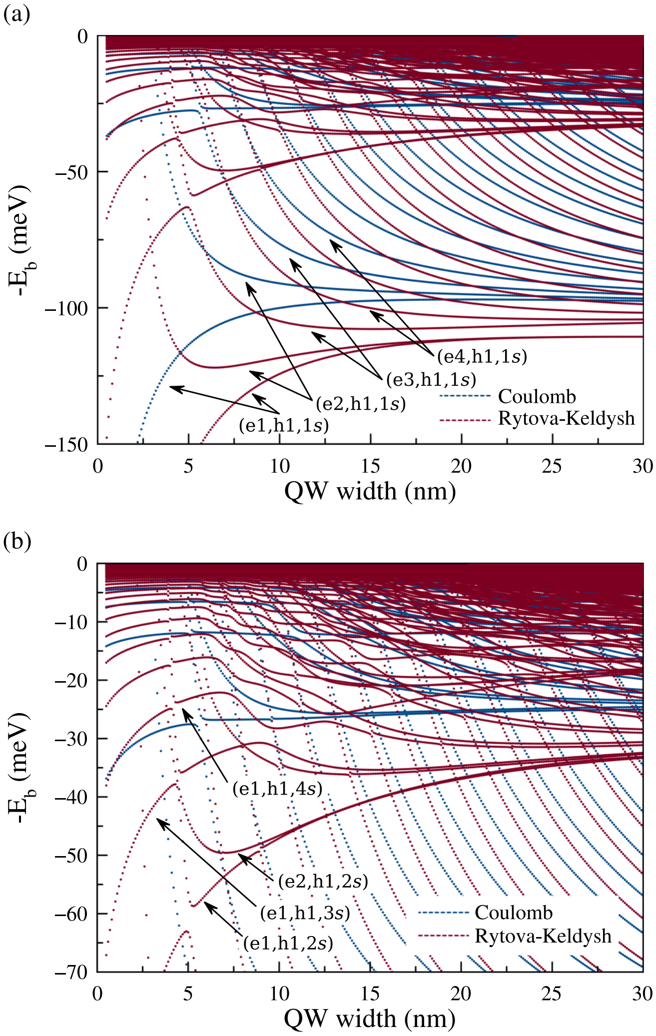

FIG. 8. (a) The comparison of energy levels of the exciton in a Cu_2O QW as a function of the QW width for $m = 0$. The energy levels are obtained with the Coulomb potential and the Rytova-Keldysh potential (with the dielectric constant in the substrate $\epsilon_b = 3$). The energy levels are labeled as (ei, hj, Ns), where i and j are the indices of the electron and hole quantum-confinement states, and N is the principal quantum number of the s-like Coulomb state. (b) Close-up of selected Rydberg energy levels.

VI. EFFECTS OF THE CRYSTAL ENVIRONMENT

So far, we used the hydrogenlike two-band model to describe the kinetic energies of the electron and hole. This model adequately reproduces the general structure of Rydberg energy levels, but does not show all the features of the spectrum such as the fine-structure splitting. If a sufficient accuracy to allow for a quantitative comparison with experiment is desired, the complex valence-band structure and other central-cell corrections for small electron-hole separations [47] have to be considered. In this section, we briefly discuss how these improvements affect the presented spectra.

A more sophisticated model for the energy dispersions of the electron and hole, that is able to properly describe the nonparabolicity of the valence bands, is given by the Suzuki-Hensel Hamiltonian, based on the Luttinger-Kohn model [40–42,46]. In this description, the treatment of the kinetic energy of the electron and hole requires the introduction of additional spin degrees of freedom, viz., the quasispin and the hole spin. With these quantities, all symmetry-compatible terms up to quadratic order in the hole momentum are included, leading to a much more complicated total Hamiltonian and an increase of the dimension of the Hilbert space by a factor of six. As a result, the computation of the fine-structure splitting due to the nonparabolic dispersion of the hole is nontrivial for highly excited Rydberg states in the transition region from weak to strong confinement.

Further complication of the model includes the central-cell corrections. They mainly affect the exciton states with principal quantum number $N = 1$, marked as $1s$ in Figs. 4–6 and 8. These states have the smallest spatial extension, and therefore most quickly reach the weak confinement region with increasing QW width. Most corrections will result in a simple shift of the energy, except for the exchange interaction, which causes a splitting of s-like states into the threefold degenerate Γ_5^+ orthoexcitons and a Γ_2^+ paraexciton [47,48,94]. The bulk $1s$ exciton is, in particular, split by about 12 meV [47]. A similar fine structure splitting is expected for the different $1s$-like states originating from the quantization in QW, i.e., there are two sequences of $1s$-like states with symmetries Γ_2^+ and Γ_5^+, respectively. For each symmetry, the spectra should be very similar (up to an energy offset) to the Rydberg series obtained with the two-band model, but for symmetry reasons in the QW, an additional splitting of the Γ_5^+ excitons into a one-dimensional and two-dimensional subspaces is expected [94].

Additionally, in the QW the translational symmetry is broken along the z direction, i.e., perpendicular to the QW plane. As a result, the associated center-of-mass momentum is no longer a conserved quantity. Thus the relative and center-of-mass coordinates cannot be introduced for all three spatial directions as in the bulk, but only in the QW plane. The rotational symmetry around the z axis is also broken by the crystal. Therefore the computation of the fine-structure splitting requires the solution of the Schrödinger equation with four degrees of freedom in coordinate space, in addition to the spin degrees of freedom related to the quasispin and hole spin. The derivation and implementation of the full Hamiltonian by using a complete basis set with, e.g., Sturmian or B-spline functions, is a highly nontrivial task. Furthermore, due to the increased size of the Hilbert space, the numerical effort for diagonalizing the Hamiltonian will grow drastically compared to the hydrogenlike two-band model for excitons in QWs.

VII. CONCLUSIONS

In this work, we have computed the energy levels of Rydberg excitons in cuprous oxide QWs of various thicknesses, ranging from weak confinement, where the effect of QW barriers can be treated as a small perturbation, to strong confinement, where the Coulomb potential degenerates into its two-dimensional counterpart. The limiting cases of weak and strong confinement can be treated by Coulomb-Sturmian and adiabatic expansion methods, respectively. However, the crossover from weak to strong confinement across ten orders of magnitude of the confinement strength can only be accurately studied by numerical methods, in our case using a finite-difference approximation or B-spline expansion methods.

We obtained the Rydberg series of energy levels in case of parabolic confinement, observed their dependence on the strength of the confinement, the crossings and avoided crossings of energies. The parabolic confinement has the distinct advantage that the variables in the Schrödinger equation are separable, and the motion of the exciton as a whole in the QW is independent of the relative *eh* motion. We observed the evolution of the energy spectrum during a crossover from weak to strong confinement, i.e., from a wide QW to a very narrow one. We observed that, due to confinement, the states that are mainly aligned along the QW plane, remain in the spectrum of bound states.

For rectangular confinement, we calculated the energy levels of excitons in Cu_2O-based quantum wells as a function of the QW width. In this case, the center-of-mass motion along the confining direction cannot be separated and one has to solve the full three-dimensional problem. The B-spline expansion of the exciton wavefunction allowed us to calculate the quantum-confinement and the Rydberg energy levels for a whole range of QW widths, including the crossover from strong to weak confinement regimes. We observed crossings and avoided crossings of energy levels and reproduced their well-known behavior in the limiting cases. We showed that the limiting models are precise in the corresponding confinement regimes, however they are unable to adequately describe the energy levels in the intermediate range of QW widths. Nonetheless, these models provide us with an insight as to how to classify the numerically obtained energy levels. We properly identified and classified several energy levels as well as explained their crossings and avoided crossings based on the symmetry properties of their quantum-confinement eigenmodes.

We additionally considered the effect of the dielectric contrast between the QW and the barrier. The smaller dielectric permittivity in the substrate causes an increase of the *eh* interaction and thus leads to larger binding energies of the states. Although our investigations using the Rytova-Keldysh potential are more related to the real experimental setup, other issues raised by the dielectric contrast, for example, a breakup of the exact parity due to the dielectric asymmetry, have to be studied in the future.

In this paper, we have used a simple two-band model to describe the kinetic energy of the electron and hole. This means that effects of the complex valence band structure on Rydberg excitons in QWs have been neglected. The accurate consideration of these effects, as outlined in Sec. VI, will be important for future detailed line-by-line comparisons between experiment and theory. Nonetheless, our results can be compared to the available experimental photoluminescence and reflectance spectra of excitons in Cu_2O-based thin films of different thicknesses. For example, a good agreement was obtained between the calculated results and the photoluminescence spectra from Ref. [19]. We believe that our data will facilitate further experimental studies and interpretation of the reflectance and photoluminescence spectra of excitons in thin films of cuprous oxide.

ACKNOWLEDGMENTS

The authors are grateful to anonymous referees and J. C. del Valle for constructive comments which significantly improved the exposition. This work was financially supported by the Deutsche Forschungsgemeinschaft through SPP 1929 GiRyd, projects SCHE 612/4-2, MA 1639/16-1, and GI 269/14-2.

APPENDIX

In Appendix, we briefly outline the numerical methods which are used to calculate the energy levels for arbitrary strength of the confinement (i.e., for arbitrary QW width).

1. Finite-difference approximation

On an equidistant grid with step size $h = \rho_{i+1} - \rho_i$, the finite-difference approximation of the second-order derivatives of Eq. (8) is given as

$$\frac{\partial^2 \Phi(z,\rho)}{\partial \rho^2} = \frac{\Phi(z,\rho_{i-1}) - 2\Phi(z,\rho_i) + \Phi(z,\rho_{i+1})}{h^2} + O(h^2).$$

The first-order derivative is approximated by

$$\frac{\partial \Phi(z,\rho)}{\partial \rho} = \frac{\Phi(z,\rho_{i+1}) - \Phi(z,\rho_{i-1})}{2h} + O(h^2).$$

Using these formulas in Eq. (8) leads to the eigenvalue problem with a five-diagonal matrix [95]. Several lowest eigenvalues of this matrix are calculated using ARPACK package [96]. As a result, the energies of the *eh* bound states for different strengths of the parabolic confinement are obtained.

2. B-spline basis expansion

The B-splines of higher orders are a more effective tool for discretizing and solving the partial differential equations than the finite-difference approximation. The unknown function is expanded over a basis of B-splines $B_i^k(x)$, $i = 1, \dots, n$, which are piecewise polynomials of degree $k-1$. Given the predefined series of the service nodes t_i, each B-spline $B_i^k(x)$ of order k is defined on the interval $[t_i, t_{i+k}]$. Values of the B-splines $B_i^k(x)$ and their derivatives at a given point x can be calculated by recursion formulas [65]

$$B_i^k(x) = \frac{x - t_i}{t_{i+k-1} - t_i} B_i^{k-1}(x) + \frac{t_{i+k} - x}{t_{i+k} - t_{i+1}} B_{i+1}^{k-1}(x),$$

$$\frac{dB_i^k(x)}{dx} = \frac{k-1}{t_{i+k-1} - t_i} B_i^{k-1}(x) - \frac{k-1}{t_{i+k} - t_{i+1}} B_{i+1}^{k-1}(x).$$

The expression for the second derivative can be derived from the above two equations.

Three important characteristics of B-splines should be highlighted. First, a B-spline of order k on an equidistant grid approximates an analytical function with accuracy of about h^k, where h is the step size of the grid. Thus higher-order B-splines give an accurate solution even for a relatively small number of nodes, which is particularly important for multidimensional problems. Second, one can choose nodes nonequidistantly and add service nodes at the boundaries in such a way as to have some B-splines equal to 1 at the boundaries, while all other B-splines are exactly zero there. Then, for example, zero boundary conditions can be easily implemented by removing the B-splines which are nonzero at the boundaries. Third, the B-splines are nonorthogonal functions, and thus the problem turns into a generalized eigenvalue problem. However, the B-spline functions have minimal support, i.e., each B-spline vanishes, $B_i^k(x) = 0$, for $x \notin [t_i, t_{i+k}]$, which significantly reduces the number of integrations to calculate matrix elements. This leads to a sparse structure of the matrices of the generalized eigenvalue problem.

When applying B-splines to represent the Hamiltonian (4) of the exciton in a QW, the following should be noted: although one applies Dirichlet boundary conditions as $\rho \to \infty$, and one can restrict the calculation domain by setting a large cutoff $\rho = \rho_{\max}$, the boundary conditions at $\rho = 0$ are less obvious. The wave function ψ should be finite, but not necessarily be zero at $\rho = 0$. To construct a zero boundary condition at $\rho = 0$, we use the substitution $\psi = \chi/\sqrt{\rho}$. As a result, the B-spline expansion of χ is employed to the Hamiltonian

$$H = -\frac{\hbar^2}{2\mu}\left(\frac{\partial^2}{\partial\rho^2} - \frac{m^2 - 1/4}{\rho^2}\right) - \frac{\hbar^2}{2m_e}\frac{\partial^2}{\partial z_e^2} - \frac{\hbar^2}{2m_h}\frac{\partial^2}{\partial z_h^2} - \frac{e^2}{\epsilon\sqrt{\rho^2 + (z_e - z_h)^2}}. \tag{A1}$$

The Coulomb interaction in this equation can be easily replaced by the Rytova-Keldysh potential (25). The zero boundary conditions over z are defined at $z_{e,h} = \pm L/2$. The constructed boundary value problem with zero boundary conditions allows one to accurately approximate the spectrum of bound states below the scattering threshold.

It is also worth noting that the fundamental solution of the in-plane radial part of Eq. (A1) is a linear combination of Bessel functions. One of these functions diverges as $\rho \to 0$. To avoid the divergence for magnetic quantum number $m = 0$, the zero boundary condition at $\rho \to 0$ was shifted to $\rho = -\varepsilon < 0$, where ε is by three orders of magnitude smaller than the smallest step of the grid. For $|m| > 0$, the divergence was not observed and no shifts were applied.

The B-spline basis expansion reads as

$$\chi(\rho, z_e, z_h) = \sum_{ijk} c_{ijk} B_i^k(\rho) B_j^k(z_e) B_k^k(z_h),$$

where the coefficients c_{ijk} form the eigenvectors of the generalized eigenvalue problem. In our calculations, we used B-splines of order $k = 5$ with equidistant nodes along the z direction and nonequidistant nodes along the ρ axis. For the nonequidistant grid, the interval between nodes scales cubically with its number. We used 30 nodes for the ρ direction and 22 nodes for each of two z coordinates. The matrix elements were calculated numerically by application of a 15 point Gauss-Kronrod formula [97]. The resulted generalized eigenvalue problem was solved by ARPACK routines [96].

---

[1] V. Fock, Zur Theorie des Wasserstoffatoms, Z. Phys. **98**, 145 (1935).

[2] L. D. Landau and L. M. Lifshitz, *Quantum Mechanics, Non-Relativistic Theory*, 3rd ed. (Butterworth-Heinemann, Oxford, 1981).

[3] T. F. Gallagher, *Rydberg Atoms* (Cambridge University Press, Cambridge, 1994).

[4] K. Sivalertporn, L. Mouchliadis, A. L. Ivanov, R. Philp, and E. A. Muljarov, Direct and indirect excitons in semiconductor coupled quantum wells in an applied electric field, Phys. Rev. B **85**, 045207 (2012).

[5] V. S. Popov and B. M. Karnakov, Hydrogen atom in a strong magnetic field, Phys.-Usp. **57**, 257 (2014).

[6] D. Wintgen and H. Friedrich, Regularity and irregularity in spectra of the magnetized hydrogen atom, Phys. Rev. Lett. **57**, 571 (1986).

[7] D. Thureja, A. Imamoglu, T. Smoleński, I. Amelio, A. Popert, T. Chervy, X. Lu, S. Liu, K. Barmak, K. Watanabe, T. Taniguchi, D. J. Norris, M. Kroner, and P. A. Murthy, Electrically tunable quantum confinement of neutral excitons, Nature (London) **606**, 298 (2022).

[8] V. Efimov, Energy levels arising from resonant two-body forces in a three-body system, Phys. Lett. B **33**, 563 (1970).

[9] S. P. Merkuriev and L. D. Faddeev, *Quantum Scattering Theory for Several Particle Systems* (Springer, Dordrecht, 1993).

[10] G. W. F. Drake, High precision theory of atomic helium, Phys. Scr. **T83**, 83 (1999).

[11] A. I. Ekimov and A. A. Onushchenko, Quantum size effect in three-dimensional microscopic semiconductor crystals, JETP Lett. **34**, 345 (1981) [Pis'ma Zh. Eksp. Teor. Fiz. **34**, 363 (1981)].

[12] J. H. Davies, *The Physics of Low-dimensional Semiconductors* (Cambridge University Press, Cambridge, 1997).

[13] Z. I. Alferov, The history and future of semiconductor heterostructures, Semiconductors **32**, 1 (1998).

[14] S. Haroche and J.-M. Raimond, *Exploring the Quantum: Atoms, Cavities, and Photons* (Cambridge University Press, Cambridge, 2006).

[15] N. G. Berloff, M. Silva, K. Kalinin, A. Askitopoulos, J. D. Töpfer, P. Cilibrizzi, W. Langbein, and P. G. Lagoudakis, Realizing the classical XY Hamiltonian in polariton simulators, Nat. Mater. **16**, 1120 (2017).

[16] F. Schäfer, T. Fukuhara, S. Sugawa, Y. Takasu, and Y. Takahashi, Tools for quantum simulation with ultracold atoms in optical lattices, Nat. Rev. Phys. **2**, 411 (2020).

[17] R. F. Kazarinov and R. A. Suris, Possibility of the amplification of electromagnetic waves in a semiconductor with a superlattice, Fiz. Tekh. Poluprovodn. **5**, 797 (1971).

[18] H. Haug and S. W. Koch, *Quantum Theory of the Optical and Electronic Properties of Semiconductors* (World Scientific, Singapore, 2009).

[19] M. Takahata, K. Tanaka, and N. Naka, Nonlocal optical response of weakly confined excitons in Cu_2O mesoscopic films, Phys. Rev. B **97**, 205305 (2018).

[20] A. L. Efros and L. E. Brus, Nanocrystal quantum dots: From discovery to modern development, ACS Nano **15**, 6192 (2021).

[21] F. Fedichkin, T. Guillet, P. Valvin, B. Jouault, C. Brimont, T. Bretagnon, L. Lahourcade, N. Grandjean, P. Lefebvre, and M. Vladimirova, Room-temperature transport of indirect excitons in AlGaN/GaN quantum wells, Phys. Rev. Appl. **6**, 014011 (2016).

[22] G. J. Ferreira, D. R. Candido, F. G. G. Hernandez, G. M. Gusev, E. B. Olshanetsky, N. N. Mikhailov, and S. A. Dvoretsky, Engineering topological phases in triple HgTe/CdTe quantum wells, Sci. Rep. **12**, 2617 (2022).

[23] D. Ahn and S. L. Chuang, Exact calculations of quasibound states of an isolated quantum well with uniform electric field: Quantum-well stark resonance, Phys. Rev. B **34**, 9034 (1986).

[24] Y. Baines, J. Buckley, J. Biscarrat, G. Garnier, M. Charles, W. Vandendaele, C. Gillot, and M. Plissonnier, Coherent tunneling in an AlGaN/AlN/GaN heterojunction captured through an analogy with a MOS contact, Sci. Rep. **7**, 8177 (2017).

[25] C. W. Clark and K. T. Taylor, Atomic hydrogen in a uniform magnetic field, Comput. Phys. Commun. **26**, 415 (1982).

[26] T. C. H. Liew, M. M. Glazov, K. V. Kavokin, I. A. Shelykh, M. A. Kaliteevski, and A. V. Kavokin, Proposal for a bosonic cascade laser, Phys. Rev. Lett. **110**, 047402 (2013).

[27] A. S. Davydow, *Quantenmechanik* (DVW, Berlin, 1967).

[28] R. Y. Kezerashvili, Few-Body systems in condensed matter physics, Few-Body Syst. **60**, 52 (2019).

[29] V. V. Kostrykin, A. A. Kvitsinsky, and S. P. Merkuriev, Faddeev approach to the three-body problem in total-angular-momentum representation, Few-Body Syst. **6**, 97 (1989).

[30] C. D. Lin, Hyperspherical coordinate approach to atomic and other Coulombic three-body systems, Phys. Rep. **257**, 1 (1995).

[31] R. Y. Kezerashvili, S. M. Tsiklauri, and A. Dublin, Trions in two-dimensional monolayers within the hyperspherical harmonics method: Application to transition metal dichalcogenides, Phys. Rev. B **109**, 085406 (2024).

[32] L. Happ, M. Zimmermann, S. I. Betelu, W. P. Schleich, and M. A. Efremov, Universality in a one-dimensional three-body system, Phys. Rev. A **100**, 012709 (2019).

[33] A. Tzimis, A. V. Trifonov, G. Christmann, S. I. Tsintzos, Z. Hatzopoulos, I. V. Ignatiev, A. V. Kavokin, and P. G. Savvidis, Strong coupling and stimulated emission in single parabolic quantum well microcavity for terahertz cascade, Appl. Phys. Lett. **107**, 101101 (2015).

[34] A. V. Trifonov, E. D. Cherotchenko, J. L. Carthy, I. V. Ignatiev, A. Tzimis, S. Tsintzos, Z. Hatzopoulos, P. G. Savvidis, and A. V. Kavokin, Dynamics of the energy relaxation in a parabolic quantum well laser, Phys. Rev. B **93**, 125304 (2016).

[35] A. Ballabio, J. Frigerio, S. Firoozabadi, D. Chrastina, A. Beyer, K. Volz, and G. Isella, Ge/SiGe parabolic quantum wells, J. Phys. D: Appl. Phys. **52**, 415105 (2019).

[36] C. Deimert, P. Goulain, J.-M. Manceau, W. Pasek, T. Yoon, A. Bousseksou, N. Y. Kim, R. Colombelli, and Z. R. Wasilewski, Realization of harmonic oscillator arrays with graded semiconductor quantum wells, Phys. Rev. Lett. **125**, 097403 (2020).

[37] F. Chen, H. Zhou, H. Li, J. Cao, S. Luo, Z. Sun, Z. Zhang, Z. Shao, F. Sun, B. Zhou, H. Dong, H. Xu, H. Xu, A. Kavokin, Z. Chen, and J. Wu, Femtosecond dynamics of a polariton bosonic cascade at room temperature, Nano Lett. **22**, 2023 (2022).

[38] E. L. Ivchenko, *Optical Spectroscopy of Semiconductor Nanostructures* (Alpha Science, Harrow, 2005).

[39] T. Kazimierczuk, D. Fröhlich, S. Scheel, H. Stolz, and M. Bayer, Giant Rydberg excitons in the copper oxide Cu_2O, Nature (London) **514**, 343 (2014).

[40] J. M. Luttinger and W. Kohn, Motion of electrons and holes in perturbed periodic fields, Phys. Rev. **97**, 869 (1955).

[41] J. M. Luttinger, Quantum theory of cyclotron resonance in semiconductors: General theory, Phys. Rev. **102**, 1030 (1956).

[42] K. Suzuki and J. C. Hensel, Quantum resonances in the valence bands of germanium. I. Theoretical considerations, Phys. Rev. B **9**, 4184 (1974).

[43] P. Grünwald, M. Aßmann, J. Heckötter, D. Fröhlich, M. Bayer, H. Stolz, and S. Scheel, Signatures of quantum coherences in Rydberg excitons, Phys. Rev. Lett. **117**, 133003 (2016).

[44] F. Schöne, S.-O. Krüger, P. Grünwald, H. Stolz, S. Scheel, M. Aßmann, J. Heckötter, J. Thewes, D. Fröhlich, and M. Bayer, Deviations of the exciton level spectrum in Cu_2O from the hydrogen series, Phys. Rev. B **93**, 075203 (2016).

[45] J. Heckötter, M. Freitag, D. Fröhlich, M. Aßmann, M. Bayer, P. Grünwald, F. Schöne, D. Semkat, H. Stolz, and S. Scheel, Rydberg excitons in the presence of an ultralow-density electron-hole plasma, Phys. Rev. Lett. **121**, 097401 (2018).

[46] F. Schweiner, J. Main, M. Feldmaier, G. Wunner, and C. Uihlein, Impact of the valence band structure of Cu_2O on excitonic spectra, Phys. Rev. B **93**, 195203 (2016).

[47] F. Schweiner, J. Main, G. Wunner, and C. Uihlein, Even exciton series in Cu_2O, Phys. Rev. B **95**, 195201 (2017).

[48] P. Rommel, J. Main, A. Farenbruch, D. R. Yakovlev, and M. Bayer, Exchange interaction in the yellow exciton series of cuprous oxide, Phys. Rev. B **103**, 075202 (2021).

[49] P. Rommel, P. Zielinski, and J. Main, Green exciton series in cuprous oxide, Phys. Rev. B **101**, 075208 (2020).

[50] J. Thewes, J. Heckötter, T. Kazimierczuk, M. Aßmann, D. Fröhlich, M. Bayer, M. A. Semina, and M. M. Glazov, Observation of high angular momentum excitons in cuprous oxide, Phys. Rev. Lett. **115**, 027402 (2015).

[51] J. Heckötter, V. Walther, S. Scheel, M. Bayer, T. Pohl, and M. Aßmann, Asymmetric Rydberg blockade of giant excitons in cuprous oxide, Nat. Commun. **12**, 3556 (2021).

[52] V. Walther, S. O. Krüger, S. Scheel, and T. Pohl, Interactions between Rydberg excitons in Cu_2O, Phys. Rev. B **98**, 165201 (2018).

[53] V. Walther, R. Johne, and T. Pohl, Giant optical nonlinearities from Rydberg excitons in semiconductor microcavities, Nat. Commun. **9**, 1309 (2018).

[54] A. Konzelmann, B. Frank, and H. Giessen, Quantum confined Rydberg excitons in reduced dimensions, J. Phys. B: At. Mol. Opt. Phys. **53**, 024001 (2020).

[55] S. A. Lynch, C. Hodges, S. Mandal, W. Langbein, R. P. Singh, L. A. P. Gallagher, J. D. Pritchett, D. Pizzey, J. P. Rogers, C. S. Adams, and M. P. A. Jones, Rydberg excitons in synthetic cuprous oxide Cu_2O, Phys. Rev. Mater. **5**, 084602 (2021).

[56] M. Takahata, K. Tanaka, and N. Naka, Superradiance-to-polariton crossover of wannier excitons with multiple resonances, Phys. Rev. Lett. **121**, 173604 (2018).

[57] A. Sekkat, M. O. Liedke, V. H. Nguyen, M. Butterling, F. Baiutti, J. d. D. Sirvent Veru, M. Weber, L. Rapenne, D. Bellet, G. Chichignoud, A. Kaminski-Cachopo, E. Hirschmann, A. Wagner, and D. Muñoz-Rojas, Chemical deposition of Cu_2O

films with ultra-low resistivity: correlation with the defect landscape, Nat. Commun. **13**, 5322 (2022).

[58] L. Trinkler, D. Dai, L. Chang, M. M.-C. Chou, T.-Y. Wu, J. Gabrusenoks, D. Nilova, R. Ruska, B. Berzina, and R. Nedzinskas, Luminescence properties of epitaxial Cu_2O thin films electrodeposited on metallic substrates and Cu_2O single crystals, Materials **16**, 4349 (2023).

[59] J. DeLange, K. Barua, A. S. Paul, H. Ohadi, V. Zwiller, S. Steinhauer, and H. Alaeian, Highly-excited Rydberg excitons in synthetic thin-film cuprous oxide, Sci. Rep. **13**, 16881 (2023).

[60] A. Neubauer, J. Heckötter, M. Ubl, M. Hentschel, B. Panda, M. Aßmann, M. Bayer, and H. Giessen, Spectroscopy of nanoantenna-covered Cu_2O: Towards enhancing quadrupole transitions in Rydberg excitons, Phys. Rev. B **106**, 165305 (2022).

[61] W. Kohn, Cyclotron resonance and de Haas-van Alphen oscillations of an interacting electron gas, Phys. Rev. **123**, 1242 (1961).

[62] F. M. Peeters, Magneto-optics in parabolic quantum dots, Phys. Rev. B **42**, 1486 (1990).

[63] E. S. Khramtsov, P. A. Belov, P. S. Grigoryev, I. V. Ignatiev, S. Y. Verbin, Y. P. Efimov, S. A. Eliseev, V. A. Lovtcius, V. V. Petrov, and S. L. Yakovlev, Radiative decay rate of excitons in square quantum wells: Microscopic modeling and experiment, J. Appl. Phys. **119**, 184301 (2016).

[64] C. De Boor, *A Practical Guide to Splines* (Springer, New York, 2001).

[65] H. Bachau, E. Cormier, P. Decleva, J. E. Hansen, and F. Martín, Applications of B-splines in atomic and molecular physics, Rep. Prog. Phys. **64**, 1815 (2001).

[66] P. A. Belov and E. S. Khramtsov, The binding energy of excitons in narrow quantum wells, J. Phys.: Conf. Ser. **816**, 012018 (2017).

[67] N. S. Rytova, The screened potential of a point charge in a thin film, Moscow Uni. Phys. Bull. **22**, 18 (1967) [Vestnik Moskovskogo Universiteta. Fiz. **22**, 30 (1967)].

[68] L. V. Keldysh, Coulomb interaction in thin semiconductor and semimetal films, JETP Lett. **29**, 658 (1979) [Pis'ma Zh. Eksp. Teor. Fiz. **29**, 716 (1979)].

[69] D. B. Tran Thoai, R. Zimmermann, M. Grundmann, and D. Bimberg, Image charges in semiconductor quantum wells: Effect on exciton binding energy, Phys. Rev. B **42**, 5906 (1990).

[70] P. A. Belov, Energy spectrum of excitons in square quantum wells, Physica E **112**, 96 (2019).

[71] P. A. Belov, Linewidths and energy shifts of electron-impurity resonant states in quantum wells with infinite barriers, Phys. Rev. B **105**, 155417 (2022).

[72] N. Moiseyev, Quantum theory of resonances: Calculating energies, widths and cross-sections by complex scaling, Phys. Rep. **302**, 212 (1998).

[73] N. Scheuler, P. Rommel, J. Main, and P. A. Belov, Resonance energies and linewidths of Rydberg excitons in Cu_2O quantum wells, Phys. Rev. B **109**, 165440 (2024).

[74] D. Bajoni, E. Peter, P. Senellart, J. L. Smirr, I. Sagnes, A. Lemaître, and J. Bloch, Polariton parametric luminescence in a single micropillar, Appl. Phys. Lett. **90**, 051107 (2007).

[75] R. Balili, V. Hartwell, D. Snoke, L. Pfeiffer, and K. West, Bose-Einstein condensation of microcavity polaritons in a trap, Science **316**, 1007 (2007).

[76] A. Amo, S. Pigeon, C. Adrados, R. Houdré, E. Giacobino, C. Ciuti, and A. Bramati, Light engineering of the polariton landscape in semiconductor microcavities, Phys. Rev. B **82**, 081301(R) (2010).

[77] E. Wertz, L. Ferrier, D. D. Solnyshkov, R. Johne, D. Sanvitto, A. Lemaître, I. Sagnes, R. Grousson, A. V. Kavokin, P. Senellart, G. Malpuech, and J. Bloch, Spontaneous formation and optical manipulation of extended polariton condensates, Nat. Phys. **6**, 860 (2010).

[78] G. Tosi, G. Christmann, N. G. Berloff, P. Tsotsis, T. Gao, Z. Hatzopoulos, P. G. Savvidis, and J. J. Baumberg, Sculpting oscillators with light within a nonlinear quantum fluid, Nat. Phys. **8**, 190 (2012).

[79] D. A. Varshalovich, A. N. Moskalev, and V. K. Khersonskii, *Quantum Theory of Angular Momentum* (Nauka, Leningrad, 1975).

[80] D. Wintgen, H. Marxer, and J. S. Briggs, Efficient quantisation scheme for the anisotropic Kepler problem, J. Phys. A: Math. Gen. **20**, L965 (1987).

[81] C. W. Clark and K. T. Taylor, The quadratic Zeeman effect in hydrogen Rydberg series: application of Sturmian functions, J. Phys. B: At. Mol. Phys. **15**, 1175 (1982).

[82] M. Abramowitz and I. A. Stegun, *Handbook of Mathematical Functions with Formulas, Graphs, and Mathematical Tables*, ninth Dover printing, tenth gpo printing ed. (Dover, New York City, 1964).

[83] J. H. Ahlberg, E. N. Nilson, and J. L. Walsh, *The Theory of Splines and Their Applications* (Academic Press, New York, 1967).

[84] P. A. Belov and S. L. Yakovlev, Asymptotic method for determining the amplitude for three-particle breakup: Neutron-deuteron scattering, Phys. Atom. Nuclei **76**, 126 (2013).

[85] J. Heckötter, M. Freitag, D. Fröhlich, M. Aßmann, M. Bayer, M. A. Semina, and M. M. Glazov, Dissociation of excitons in Cu_2O by an electric field, Phys. Rev. B **98**, 035150 (2018).

[86] E. Anderson, Z. Bai, C. Bischof, L. S. Blackford, J. Demmel, J. J. Dongarra, J. Du Croz, S. Hammarling, A. Greenbaum, A. McKenney, and D. Sorensen, *LAPACK Users' Guide (3rd ed.)* (Society for Industrial and Applied Mathematics, Philadelphia, 1999).

[87] P. Duclos, P. Šťovíček, and M. Tušek, On the two-dimensional Coulomb-like potential with a central point interaction, J. Phys. A: Math. Theor. **43**, 474020 (2010).

[88] A. Chernikov, T. C. Berkelbach, H. M. Hill, A. Rigosi, Y. Li, B. Aslan, D. R. Reichman, M. S. Hybertsen, and T. F. Heinz, Exciton binding energy and nonhydrogenic Rydberg series in monolayer WS_2, Phys. Rev. Lett. **113**, 076802 (2014).

[89] R. Y. Kezerashvili and S. M. Tsiklauri, Trion and biexciton in monolayer transition metal dichalcogenides, Few-Body Syst. **58**, 18 (2017).

[90] P. Cudazzo, I. V. Tokatly, and A. Rubio, Dielectric screening in two-dimensional insulators: Implications for excitonic and impurity states in graphane, Phys. Rev. B **84**, 085406 (2011).

[91] J. C. del Valle, J. A. Segura Landa, and D. J. Nader, Two- and three-particle complexes with logarithmic interaction: Compact wave functions for two-dimensional excitons and trions, Phys. Rev. B **108**, 155421 (2023).

[92] F. García Flórez, L. D. A. Siebbeles, and H. T. C. Stoof, Effects of material thickness and surrounding dielectric medium on

Coulomb interactions and two-dimensional excitons, Phys. Rev. B **102**, 125303 (2020).

[93] M. N. Polyanskiy, Refractiveindex.info database of optical constants, Sci. Data **11**, 94 (2024).

[94] G. Koster, J. Dimmock, R. Wheeler, and H. Statz, *Properties of the Thirty-Two Point Groups*, Massachusetts institute of technology press research monograph (M.I.T. Press, Cambridge, 1963).

[95] P. A. Belov, E. R. Nugumanov, and S. L. Yakovlev, The arrowhead decomposition method for a block-tridiagonal system of linear equations, J. Phys.: Conf. Ser. **929**, 012035 (2017).

[96] R. B. Lehoucq, D. C. Sorensen, and C. Yang, *ARPACK Users' Guide* (Society for Industrial and Applied Mathematics, Philadelphia, 1998).

[97] D. Kahaner, C. Moler, and S. Nash, *Numerical Methods and Software* (Prentice Hall, Englewood Cliffs, 1989).